

Influence of Region-dependent Error Growth on the Predictability of Tropical Cyclone Track and Intensity in High-resolution HWRF Ensembles

Jie Feng¹, Falko Judt², and Jing Zhang³

¹Department of Atmospheric and Oceanic Sciences, Fudan University

²National Center for Atmospheric Research

³Shanghai Typhoon Institute, China Meteorological Administration

June 1, 2023

Abstract

Further extension of skillful prediction of tropical cyclones (TCs) relies on in-depth studies about the intrinsic predictability of TCs. In this study, convection-resolving ensemble forecasts based on the Hurricane Weather Research and Forecasting model were adopted with perturbed initial conditions to study the error growth and intrinsic predictability of TCs. The new aspect of our study is the focus on the sensitivity of TC track and intensity predictability to initial errors in different regions, including (1) the inner core and outer rainbands (0-350 km), (2) the near environment (350-1300 km), and (3) the far environment (1300-3500 km).

The results of TC track predictability show that the most sensitive region of initial errors for TC track forecasts is case-dependent. For the TC case with striking track forecast errors (e.g., Typhoon Chan-hom, 2020), the initial errors in the combined region of the TC inner core and outer rainbands produce the largest track uncertainties compared to those in the near and far environment. However, for the TC case with a highly predictable track (e.g., Typhoon Maysak, 2020), the most sensitive region of initial errors is the near environment at early lead times and the far environment later. By contrast, the most sensitive region for TC intensity is the inner core for both cases. The surface wind structure of TC inner core at larger scales (wavenumbers 0-2) can be predicted for more than 3.5 days, while the structure at smaller scales can only be predicted for a few hours.

Hosted file

964215_0_art_file_11030569_rvb7ht.docx available at <https://authorea.com/users/624010/articles/646510-influence-of-region-dependent-error-growth-on-the-predictability-of-tropical-cyclone-track-and-intensity-in-high-resolution-hwrf-ensembles>

1
2 **Influence of Region-dependent Error Growth on the Predictability of Tropical**
3 **Cyclone Track and Intensity in High-resolution HWRF Ensembles**
4

5 **Jie Feng^{1,2*}, Falko Judt³, Jing Zhang^{4*}**

6
7 ¹*Department of Atmospheric and Oceanic Sciences and Institute of Atmospheric Sciences, Fudan*
8 *University, Shanghai, China*

9 ²*Shanghai Qi Zhi Institute, Shanghai, China*

10 ³*Mesoscale and Microscale Meteorology Laboratory, National Center for Atmospheric*
11 *Research, Boulder, CO, USA*

12 ⁴*Shanghai Typhoon Institute, China Meteorological Administration, Shanghai, China*
13

14
15 Corresponding author: Jie Feng (fengjie@fudan.edu.cn) ; Jing Zhang (zhangj@typhoon.org.cn)
16

17
18
19 **Key Points:**

- 20
- 21 • The most sensitive region of initial errors for TC track uncertainties is not always in the environment but maybe within a TC.
 - 22 • Uncertainties in TC intensity are most sensitive to initial errors in the TC inner core.
 - 23 • The source of TC intensity predictability for a few days is the predictable environment.
- 24

25
26
27
28
29
30
31
32
33
34
35
36
37
38
39
40
41
42
43
44
45
46
47
48
49
50
51
52
53
54
55
56
57
58
59
60

Abstract

Further extension of skillful prediction of tropical cyclones (TCs) relies on in-depth studies about the intrinsic predictability of TCs. In this study, convection-resolving ensemble forecasts based on the Hurricane Weather Research and Forecasting model were adopted with perturbed initial conditions to study the error growth and intrinsic predictability of TCs. The new aspect of our study is the focus on the sensitivity of TC track and intensity predictability to initial errors in different regions, including (1) the inner core and outer rainbands (0-350 km), (2) the near environment (350-1300 km), and (3) the far environment (1300-3500 km).

The results of TC track predictability show that the most sensitive region of initial errors for TC track forecasts is case-dependent. For the TC case with striking track forecast errors (e.g., Typhoon Chan-hom, 2020), the initial errors in the combined region of the TC inner core and outer rainbands produce the largest track uncertainties compared to those in the near and far environment. However, for the TC case with a highly predictable track (e.g., Typhoon Maysak, 2020), the most sensitive region of initial errors is the near environment at early lead times and the far environment later. By contrast, the most sensitive region for TC intensity is the inner core for both cases. The surface wind structure of TC inner core at larger scales (wavenumbers 0-2) can be predicted for more than 3.5 days, while the structure at smaller scales can only be predicted for a few hours.

Plain Language Summary

The prediction of tropical cyclones (TCs) has progressively improved in the past few decades. How long can we further extend skillful TC prediction? The answer to this question relies on in-depth studies about TC intrinsic predictability. In this study, the HWRF-based convection-resolving ensemble forecasts were adopted with perturbed initial conditions to study the error growth and intrinsic predictability of TCs. The new aspect of our study is the focus on the sensitivity of TC track and intensity predictability to initial errors in different regions. The main conclusions include: (1) the most sensitive region of initial errors for TC track uncertainties is case-dependent and not always in the environment. The initial errors in the combined region of TC inner core and outer rainbands may produce much larger track errors than those in the near and far environments for TCs with low track predictability. (2) For TC intensity, the most sensitive region consistently locates within the TC inner core. The large-scale components (wavenumber 0-2) of TC inherent vortex flow can be predicted for more than 3.5 days, which is primarily attributed to the predictability of the synoptic-scale environment. By contrast, the remaining components (wavenumber >2) are only predictable for a few hours.

61 **1 Introduction**

62 The prediction of tropical cyclones (TCs) remains challenging despite recent progress in
63 theory, observing systems, numerical models, and data assimilation. The intensity of TCs is a
64 crucial indicator of their disaster potential and is one of the most difficult metrics to predict as a
65 result of the complex multi-scale interactions in TCs (e.g., Wang and Wu, 2004; Gopalakrishnan
66 et al., 2011). As is well known, the errors in forecasting TC intensity have only decreased at a
67 slow rate during the last few decades (Cangialosi and Franklin, 2014; DeMaria et al., 2014). By
68 contrast, the errors in forecasting the tracks of TCs have significantly decreased by more than
69 half within the same time period (Katz and Murphy, 2015). Despite this improvement in
70 predicting TC tracks, there can still be remarkable errors in the prediction of TC tracks,
71 especially those with curving, looping, or stalling paths (e.g., Wu et al., 2014; Torn et al., 2015;
72 Feng et al., 2022). The increasing difficulties in continuously lowering TC track and intensity
73 forecast errors prompt fundamental questions about their intrinsic predictability.

74 It is widely recognized that the track of a TC is primarily determined by the large-scale
75 environmental steering flow (e.g., Emanuel et al., 2004; Wu et al., 2005) and generally defined
76 as the regional and multi-layer mean of the wind fields (Holland, 1993). The steering flow
77 represents weather systems that surround a TC, such as the monsoon trough, the subtropical
78 ridge, and the mid-latitude trough (e.g., Chia and Ropelewski, 2002; Wu et al., 2005). From the
79 perspective of predictability, many studies have shown that errors in the structures and positions
80 of these synoptic-scale systems give rise to errors in TC tracks (e.g., Ito and Wu, 2013; Torn et
81 al., 2018; Ashcroft et al., 2021; Hazelton et al., 2023). For example, Nystrom et al. (2018) found
82 that the dominant source of track errors for Hurricane Joaquin (2015) arose from the
83 environmental region >300 km from the TC center based on an ensemble-based sensitivity
84 analysis. Other studies have shown that the errors associated with the internal processes in a TC
85 may produce significant differences in the TC environments, which then feed back into errors in
86 the track (e.g., Anwender et al., 2008; Harr et al., 2008; Torn et al., 2015). The sensitivity of
87 track forecasts to initial condition errors in specific regions remains a topic of disagreement, and
88 there has been limited investigation into how this sensitivity may vary on a case-by-case basis.

89 Predicting TC intensity is more challenging than predicting TC tracks as a result of the
90 complex interactions of dynamic and thermodynamic processes at multiple spatiotemporal scales
91 (e.g., Wang and Wu, 2004; Gopalakrishnan et al., 2011). Decades of research have shown that
92 TC intensity are affected by the large-scale environment, such as the vertical wind shear (e.g.,
93 Black et al., 2002; Chen et al., 2006; Tang and Emanuel, 2012, Rios-Berrios and Torn, 2017), the
94 temperature and salinity of the upper ocean (e.g., Emanuel et al., 2004), and air–sea interactions
95 (Emanuel, 1986; Chen et al., 2007, 2013; Ma et al., 2017, 2018). In addition to these
96 environmental factors, the effects of internal mesoscale processes on the TC intensity have also
97 been highlighted, including the eyewall convection, adiabatic warming of the inner core, and
98 secondary eyewall replacement (e.g., Shapiro and Willoughby, 1982; Rogers, 2010; Zhang and
99 Chen, 2012; Qin et al., 2021, 2023). The intricate interplay between the internal and
100 environmental structures of TCs and the modulation of their spiral rainbands and secondary
101 circulation has been widely documented (e.g., Houze et al., 2006; Judt and Chen, 2010, Li and
102 Wang, 2012). These complex interactions can make it challenging to predict changes in TC
103 intensity, and the question about the regions in which the physical processes dominantly control
104 the TC intensity remains at the center of their predictability.

105 The predictability of the TC intensity is often examined by analyzing the sensitivity of
106 the predictions of TC intensity and structure to discrepancies in the initial conditions. Sipple and
107 Zhang (2008, 2010) showed that the initial errors associated with moist convection, even those
108 with negligible magnitudes, increase rapidly and contaminate other physical processes at larger
109 scales through the upscaling error growth, which severely limits the predictability of the TC
110 intensity. Van Sang et al. (2008) and Shin and Smith (2008) concluded that small initial random
111 perturbations of moisture in the boundary layer can cause strong asymmetries in the TC vortex,
112 resulting in a larger spread of intensity. In addition to the limitation of predictability due to TC
113 inner core processes alone, some studies have shown that the predictability of the TC intensity
114 decreases (i.e., becomes more sensitive to initial uncertainties) when vertical wind shear
115 increases (Zhang and Tao, 2013; Tao and Zhang, 2015; Finocchio and Majumdar, 2017). Judt
116 and Chen (2016) found that complex interactions among the vertical wind shear, the mean
117 vortex, and internal convective processes jointly contribute to uncertainties in the TC intensity.
118 Although the sensitivity of TC intensity forecasts to multiple factors has been intensively
119 explored, the relative sensitivity of the TC intensity to the initial errors in different regions has
120 not been addressed explicitly.

121 There have been a few studies quantifying the upper bound of the predictability of the TC
122 intensity. Kieu and Moon (2016) reported that the sample-mean forecast errors of the TC
123 intensity measured by the maximum sustained surface wind (MSW) speed approach a saturation
124 value of about $8\text{--}10\text{ m s}^{-1}$ in an axisymmetrical model and real-time data statistics. With this
125 threshold, they gave an upper limit for the predictability of the MSW of about three days. Hakim
126 (2013) derived a similar predictability limit of about three days for the azimuthal wind using
127 analog forecasts based on long-range simulation data for an idealized axisymmetrical model.
128 Kieu and Rotunno (2022) found that the spectral kinetic error growth for azimuthal
129 wavenumbers reaches saturation after ~ 9 hr as compared to ~ 18 hr for the radial direction in an
130 idealized simulation of TC. Zhong et al. (2018) estimated a possible range of two and a half to
131 seven days for the TC intensity predictability over the western North Pacific basin using a local
132 dynamic analog method. Their results, however, relied on simplified tropical cyclone models or
133 algorithms in an ideal framework without considering the effect of multi-scale physical processes
134 on the change in TC intensity.

135 Judt et al. (2016) investigated the scale-dependent predictability limits of the inner core
136 surface winds of TCs in the cloud-resolving Weather Research and Forecasting (WRF) model
137 using Fourier decomposition. They found that the error growth and the predictability limits of the
138 surface wind speed were scale-dependent: (1) the mean vortex and wavenumber-1 asymmetry
139 were predictable for > 7 days; (2) the scales associated with rain bands (wave numbers 2–5) were
140 predictable for a few days; and (3) convective scales (wave numbers >7) were only predictable
141 for 6–12 hrs. However, because Judt et al. (2016) used a stochastic perturbation method that
142 mimics model error and continuously perturbed the model fields, they could not address the
143 question of the intrinsic predictability of TCs—that is, the extent to which prediction is possible
144 if an almost perfect procedure is used (e.g., Lorenz, 1969; Sun and Zhang, 2016; Selz, 2019).
145 Furthermore, Judt et al. (2016) only used a single case, and therefore did not explore the case
146 dependence of the predictability of TC track and intensity .

147 In response to the limitations mentioned above, the present study aims to investigate the
148 intrinsic predictability of the TC track and intensity using convection-resolving ensemble
149 forecasts with perturbed initial conditions based on the Hurricane Weather Research and

150 Forecasting (HWRF) model for two distinct cases. To assess the varying sensitivity of track and
151 intensity forecasts to different regions of initial errors, we investigated the error growth and
152 dynamics of such region-dependent errors. We investigated Typhoons (TCs occurred in the
153 Western Pacific) Chan-hom and Maysak in 2020, two cases that turned out to have very distinct
154 track predictabilities. A comparison of the results for these two TCs will help to clarify the case
155 dependence of the TC predictability.

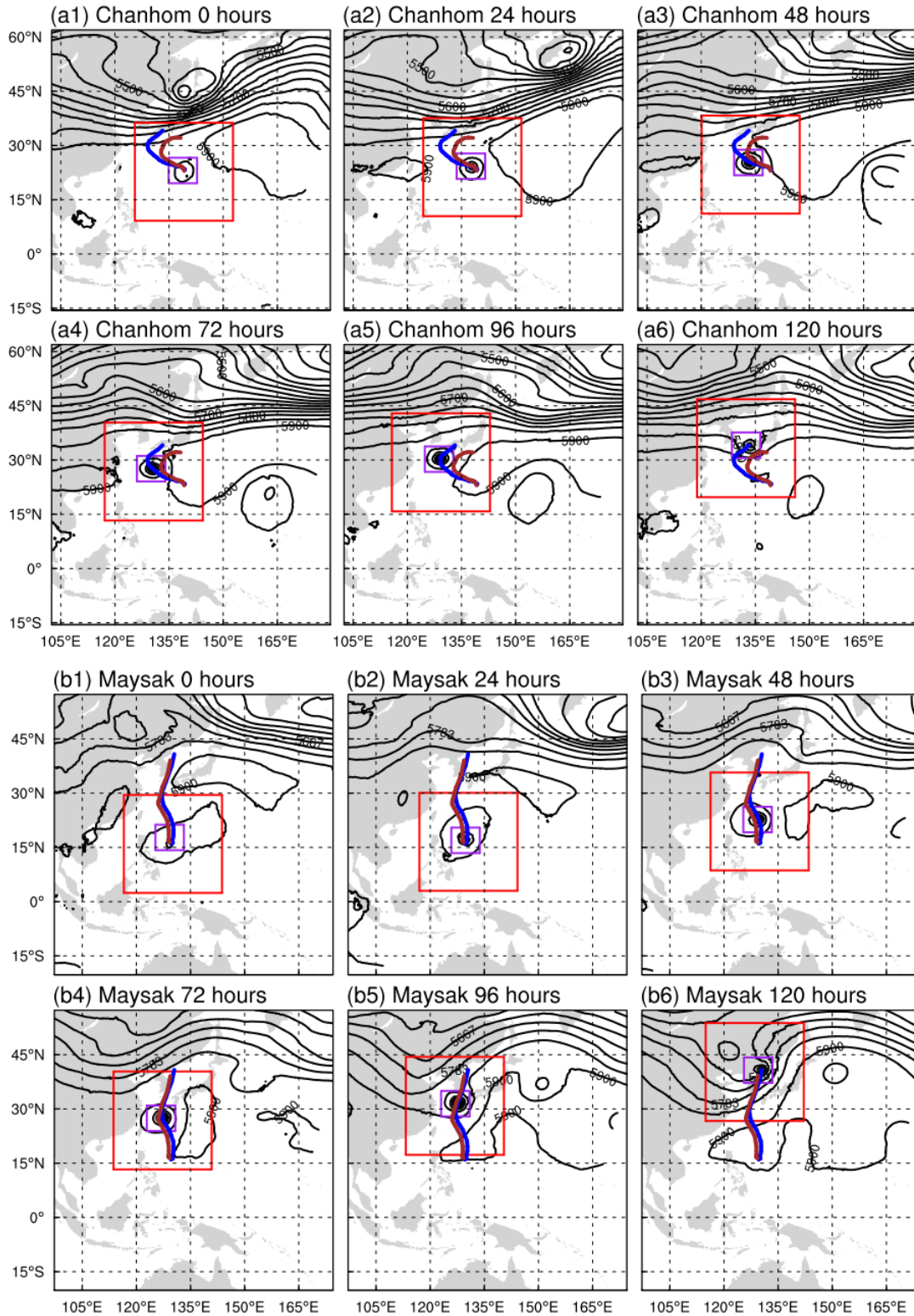
156 This paper is organized as follows. Section 2 describes the model setup. Section 3
157 provides a brief review of the two typhoons and introduces the experimental design. The results
158 of the intrinsic predictability analysis are presented and discussed in Sections 4 (track) and 5
159 (intensity). Section 6 discusses the results of the combined effect of the initial and boundary
160 uncertainties on the predictability of TCs. Finally, Section 7 presents our conclusions and
161 discussion.

162

163 **2 Model setup**

164 The ensemble forecasts used in our predictability analyses were generated using the latest
165 version of the regional high-resolution HWRF model (version 4.0a). The HWRF model has been
166 widely used for both operational forecasts and research of tropical storms (e.g., Lu et al., 2017;
167 Zhang et al., 2016; Zhang et al., 2018; Feng et al., 2019, 2021). The HWRF model is configured
168 with triply nested domains, including an innermost convection-resolving grid at 2 km horizontal
169 resolution (D03; Fig. 1, purple box) and an intermediate grid at 6 km resolution (D02; Fig. 1, red
170 box), enclosed by the stationary outer domain at 18 km resolution (D01; Fig. 1, outermost
171 domain). The inner two domains (D02 and D03) follow the vortex to ensure that the TC stays in
172 the domain with the highest resolution. The three domains roughly cover an area of $77^{\circ}\times 77^{\circ}$ for
173 D01 (288×576 grid points), $27^{\circ}\times 27^{\circ}$ for D02 (304×604 grid points), and $7^{\circ}\times 8^{\circ}$ for D03
174 (265×472 grid points), with 61 vertical levels up to 2 hPa.

175 Convective processes for the two outer domains with resolutions of 18 and 6 km were
176 parameterized using the simplified Arakawa–Schubert cumulus scheme (Han and Pan, 2006), but
177 were simulated explicitly for the innermost domain at 2 km grid spacing. The effect of moist
178 physical processes was simulated using the Ferrier–Aligo microphysics scheme (Ferrier, 1994,
179 2005). Other model physics schemes included the modified surface layer (Kwon et al., 2010) and
180 non-local planetary boundary layer (Hong and Pan, 1996) parameterization schemes, and the Eta
181 Geophysical Fluid Dynamics Laboratory longwave and shortwave radiation schemes
182 (Schwarzkopf and Fels, 1991; Lacis and Hansen, 1974).



183

184 Figure 1. Evolution of the 500 hPa geopotential height in D01 for (a1–a6) Typhoon Chan-hom
 185 and (b1–b6) Typhoon Maysak during the control experiment from 0 to 120 h at intervals of 24 h

186 overlain by the tracks of the control (dark blue) and best-track observations (brown) within the
187 same time period. The red and purple squares highlight areas D02 and D03.

188

189 3 Experimental setup

190 3.1 Review of the tropical cyclones

191 The two typhoons selected for this study were Typhoon Chan-hom, which occurred in
192 early October 2020; and Typhoon Maysak, which lasted from the end of August to early
193 September 2020. These two typhoons had remarkably different forecast uncertainty associated
194 with their tracks (Fig. 1). The observed Typhoon Chan-hom intensified into a tropical storm (TS)
195 at about 12 UTC on 5 October 2020 (i.e., the initial time of the forecasts in Fig. 1) and then
196 moved northwestward and gradually turned toward the southern mainland of Japan. On 8
197 October, Typhoon Chan-hom turned sharply to the east while approaching peak intensity and
198 then moved to the northeast off the eastern coast of Japan. The sharp turn to the east proved
199 challenging for our five-day forecast experiment, and the simulated storm in the control run
200 ended up turning too late and made landfall in Japan (*cf.* Fig. 1(a1–a6), blue and purple curves).
201 By contrast, Typhoon Maysak’s control forecast had smaller track forecast errors (<100 km) and
202 featured much less uncertainty. This may have been associated with its stable northward motion
203 from the East China Sea to landfall in South Korea.

204 The varying levels of forecast accuracy and associated uncertainties for the tracks of
205 Typhoons Chan-hom and Maysak in both the control forecasts and observed outcomes suggest
206 differing predictability for each. By comparing these two typhoons, we aim to gain a better
207 understanding of the case-dependent sensitivity of initial errors in predicting the track and
208 intensity of tropical cyclones. Notably, both Chan-hom and Maysak experienced prolonged
209 lifetimes (lasting five to six days) over open waters without topographic influences. Moreover,
210 they both maintained at least tropical storm intensity throughout their lifetime and eventually
211 intensified into typhoons with maximum sustained winds exceeding 40 m s^{-1} .

212 3.2 Definition of the regions where perturbations will be introduced

213 As the main goal of our study was to investigate the intrinsic sensitivity of the TC track
214 and intensity to region-dependent initial uncertainties, we used the three nested domains to
215 roughly divide the structure and characteristics of TCs into three regions (Fig. 1 and Table 1).
216 The innermost domain (i.e., D03) covers the TC inner core¹ and the outer spiral rainbands within
217 about 350 km of the TC center almost five to six times the radius of the maximum wind. The
218 region referred to in Table 1 as “part of D03” is also defined to investigate the role of the TC
219 inner core (0–250 km) and the outer rainbands (250–350 km). The region between the innermost
220 and intermediate domains (i.e., D02 and D03) from about 350 to 1300 km roughly corresponds
221 to the environment adjacent to the TC vortex (defined as the near environment). The region
222 between the intermediate and outer domains (i.e., D02 and D01) from 1300 to 3500 km roughly
223 overlies the synoptic-scale weather systems at a long distance from the TC center (defined as the
224 far environment).

¹The inner core region of a strong TC generally includes the eye, eyewall, and the principle rain bands within about three times the radius of the maximum wind (Houze, 2010).

225 Table 1. Definitions of the regions in a tropical cyclone and their ranges and characteristics.

Region	Range (km)	Characteristics
D03	0–350	Inner core and outer rainbands
D03 to D02	350–1300	Near environment
D02 to D01	1300–3500	Far environment
Part of D03	0–250	Inner core
	250–350	Outer rainbands

226

227 3.3 Experimental design

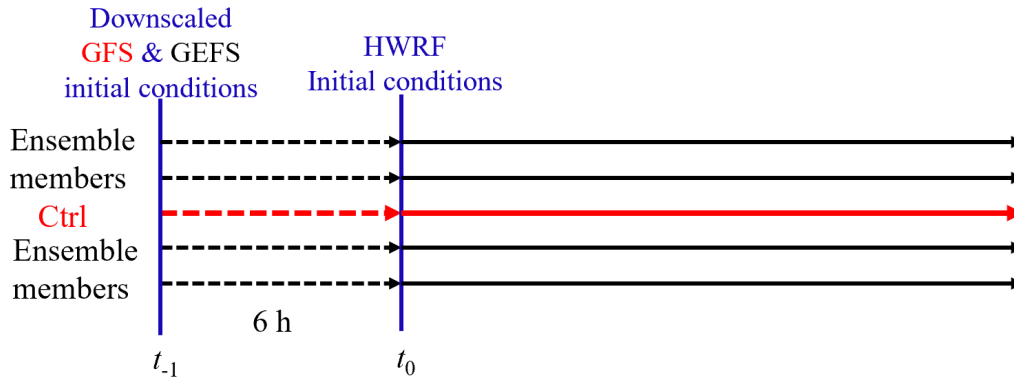
228 Fig. 2 shows a flow diagram of the experiment. The first step is to generate the initial
 229 control and perturbed ensemble conditions ($N = 20$) valid at time t_0 for the three nested domains
 230 in the HWRF model. The initial conditions are 6-hr HWRF forecasts from time t_{-1} to t_0
 231 initialized with the downscaled fields of the control analysis of the Global Forecast System
 232 (GFS, 0.25° resolution) and the perturbed analyses of the Global Ensemble Forecast System
 233 (GEFS, 0.5° resolution; Zhou et al., 2022) from the National Centers for Environment
 234 Prediction. The GFS forecasts provide the lateral boundary conditions for the 6-h HWRF control
 235 (red dashed arrow) and ensemble (black dashed arrow) forecasts, respectively. We use the 6-h
 236 short-term HWRF forecasts as the initial conditions instead of the downscaled GFS/GEFS fields
 237 to start the simulations with more realistic dynamically evolved and spatially coherent initial
 238 ensemble perturbations.

239 Once the initial control and ensemble conditions for the HWRF model are created, the
 240 second step is the design of numerical experiments to address the impact of the region-dependent
 241 initial errors on the TC predictability. The HWRF model adopts two-way communication for
 242 multiple nested domains in which the time- and space-interpolated values of the parent domain
 243 are specified on the nest boundaries while the inner domain is advanced (Moeng et al., 2007).
 244 The interior values of the nest domain are then transferred to the parent domain, overwriting the
 245 parent domain solution in the overlapped region. Perturbing the control analyses in D01, D02,
 246 and D03, therefore, introduces the initial errors associated with the far environment (but not the
 247 near environment nor the inner core and outer rainbands), the near environment (but not the far
 248 environment nor the inner core and outer rainbands), and the inner core and outer rainbands,
 249 respectively (Table 1).

250 Based on this concept, we defined the numerical experiments as follows (see Table 2).
 251 The baseline experiment (the Ctrl experiment) is the control analyses and forecasts (red solid
 252 arrow in Fig. 2). Experiment PertD01 uses the perturbed initial ensemble for D01, but the initial
 253 conditions for D02 and D03 are the same as in the Ctrl experiment. Similarly, experiments
 254 PertD02 and PertD03 simply perturb the initial conditions for D02 and D03, respectively. To
 255 determine the individual effects of uncertainties in the inner core and outer rainbands of the TC,
 256 experiments PertD03-Vor and PertD03-Rainb are carried out with the initial perturbations
 257 superposed on a smaller region than in PertD03—that is, the inner core and outer rainband

258 regions, respectively. These experiments (PertD01, PertD02, PertD03, PertD03-Vor, and
 259 PertD03-Rainb) use the same lateral boundaries as the Ctrl experiment to display the effects
 260 related to the initial error. Experiment PertAll retains all the perturbations in the initial ensemble
 261 of the three nested domains and the lateral boundaries.

262 The third step is to integrate the initial control and ensemble conditions from t_0 for all
 263 experiments for five days using the HWRF model with the output at intervals of 6 h. The initial
 264 time t_0 is the point at which the two typhoons reached TS intensity of nearly 18 m s^{-1} , i.e., 1200
 265 UTC on 5 October 2020 for Typhoon Chan-hom and 0000 UTC on 29 August 2020 for Typhoon
 266 Maysak.



267

268 Figure 2. Schematic diagram of the experimental flow. GFS, Global Forecast System; GEFS,
 269 Global Ensemble Forecast System.

270 Table 2. Descriptions of the control (Ctrl) and ensemble forecast experiments.

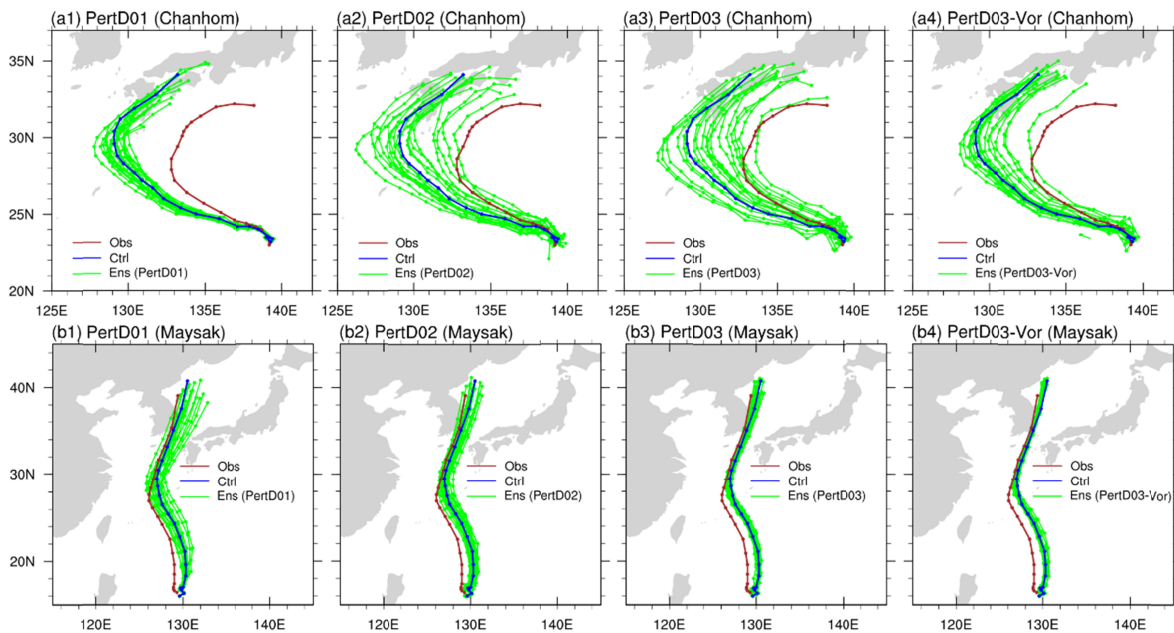
	Ctrl	PertD01	PertD02	PertD03	PertD03-Vor	PertD03-Rainb	PertAll
D01 perturbed	No	Yes	No	No	No	No	Yes
D02 perturbed	No	No	Yes	No	No	No	Yes
D03 perturbed	No	No	No	Yes	Yes, vortex (0–250 km)	Yes, outer rainbands (250–350 km)	Yes
Boundary perturbed	No	No	No	No	No	No	Yes

271

272 4 Intrinsic predictability of the track of tropical cyclones

273 4.1 Track uncertainty

274 Fig. 3 shows the five-day ensemble track forecasts (green curves) for the two typhoons
 275 for experiments PertD01 (Fig. 3a1, b1), PertD02 (Fig. 3a2, b2), PertD03 (Fig. 3a3, b3), and
 276 PertD03-Vor (Fig. 3a4, b4) overlain with the TC tracks from the Ctrl experiment and the
 277 observations (blue and brown curves, respectively). Note that the ensemble track forecasts are
 278 compared with the Ctrl experiment rather than the observations in all subsequent analyses. As
 279 pointed out in Fig. 1, the Ctrl track errors of Typhoon Chan-hom when verified against the
 280 observations are significantly larger than those of Typhoon Maysak, which is consistent with the
 281 much larger spread of the ensemble track of Typhoon Chan-hom than that of Typhoon Maysak.
 282 This probably indicates the different intrinsic predictabilities of the two typhoons—that is, the
 283 track of Typhoon Maysak is inherently more predictable than that of Typhoon Chan-hom. The
 284 ensemble track spread exhibits striking variations among the experiments for each typhoon,
 285 indicating their contrasting sensitivities to the initial uncertainty regions.

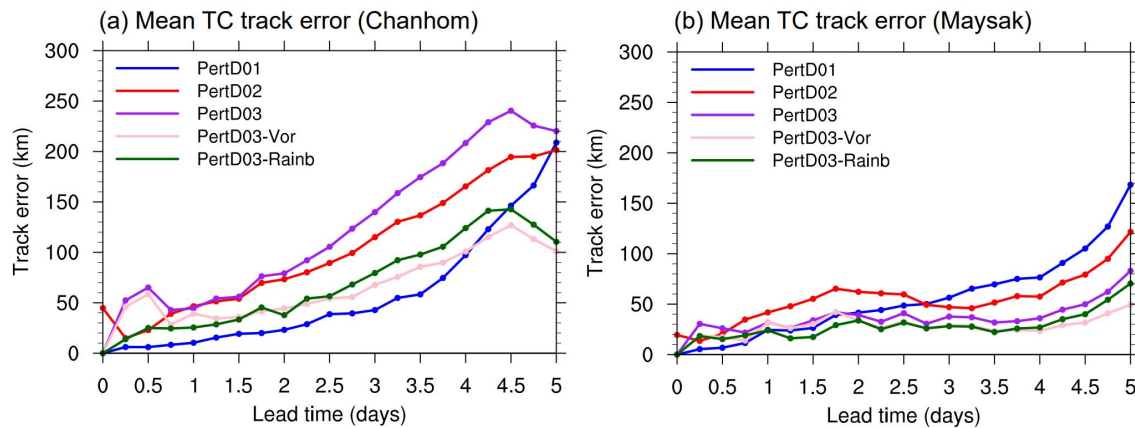


286
 287 Figure 3. Five-day tracks in the Ctrl forecast (dark blue), observations (brown), and the ensemble
 288 forecasts (green) of (a1) PertD01, (a2) PertD02, (a3) PertD03, and (a4) PertD03-Vor for
 289 Typhoon Chan-hom and (b1) PertD01, (b2) PertD02, (b3) PertD03, and (b4) PertD03-Vor for
 290 Typhoon Maysak.

291
 292 Fig. 4 further quantifies the ensemble track errors verified against the Ctrl forecast
 293 averaged over all ensemble members for Typhoons Chan-hom and Maysak. For Typhoon Chan-
 294 hom (Fig. 4a), PertD03 with initial errors in D03 shows the largest track errors at all lead times,
 295 followed by PertD02 and PertD01 with initial errors in the near and far environments,
 296 respectively. Noticeably, the comparison of PertD03 with PertD03-Vor and PertD03-Rainb
 297 shows that the mean TC track error is significantly reduced when the uncertainties in the outer
 298 rainband or the inner core region of the TC are removed. This interesting result may indicate that
 299 the high sensitivity of the TC track to initial errors in D03 is contributed to a large degree by the
 300 strong interaction of errors in the inner core and the outer rainbands (or the environment

301 interface in other words) of the TC (Houze, et al., 2006; Li and Wang, 2012) (see more details in
302 Fig. 6).

303 By contrast, despite the smaller track errors overall, Typhoon Maysak shows qualitatively
304 different results from Typhoon Chan-hom (*cf.* Fig. 4a and 4b), suggesting that the initial errors in
305 the TC environment induce the largest track forecast errors. The most sensitive region is the near
306 environment (i.e., PertD02) during the first 2.5 days, followed by the far environment (i.e.,
307 PertD01) for longer lead times. The comparison between Typhoons Chan-hom and Maysak
308 suggests that the track errors for a TC with a low track predictability may be most sensitive to the
309 initial uncertainties in the combined region of the inner core and outer rainband. By contrast, the
310 track errors in a highly predictable TC may be most sensitive to the near environment in the
311 earlier stages and then the outer environment for long-range predictions. The high track
312 predictability is possibly associated with the weak interactions between the inner core and the
313 outer rainband and environment (see Fig. 7 for more details).

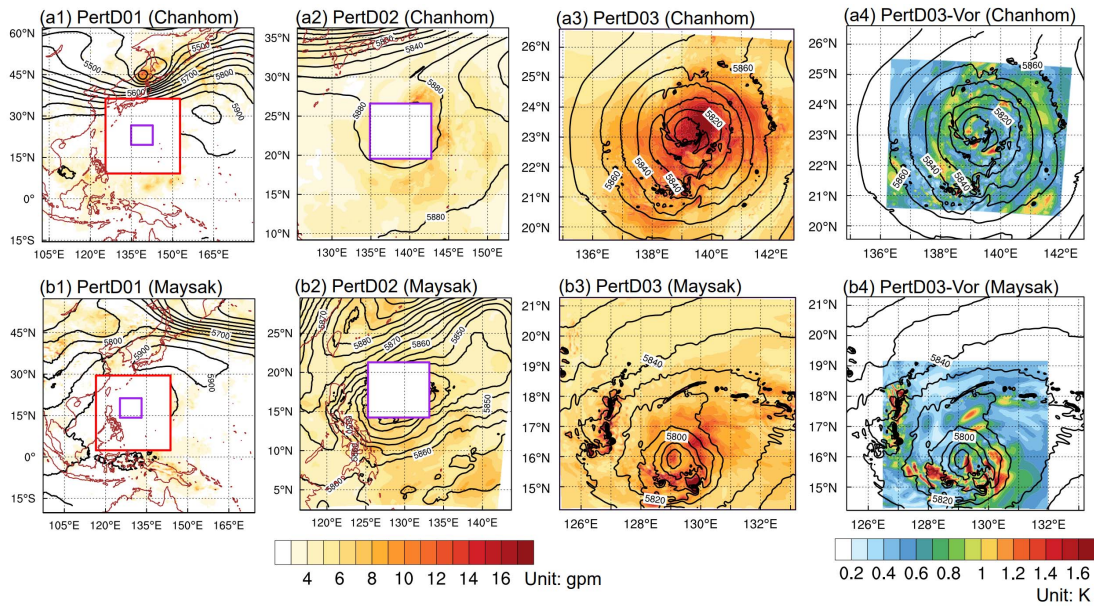


314
315 Figure 4. Track errors of the ensemble forecasts against the Ctrl forecast averaged over all
316 ensemble members in PertD01 (dark blue), PertD02 (red), PertD03 (purple), PertD03-Vor (pink),
317 and PertD03-Rainb (dark green) for Typhoons (a) Chan-hom and (b) Maysak.

318

319 4.2 Growth of region-dependent initial errors

320 To explore how region-specific initial errors lead to diverse outcomes in the predictability
321 of TC tracks, we examined the ensemble-averaged error growth of the 500-hPa geopotential
322 height (GH) and temperature (T) fields for different experiments. Fig. 5 shows the ensemble-
323 averaged initial errors in the 500-hPa GH for D01 of PertD01, D02 of PertD02, and D03 of
324 PertD03. The ensemble-averaged initial error of the 500-hPa T for D03 of PertD03-Vor is shown
325 in Figs. 5a4 and 5b4 because the initial ensemble perturbations between the 250 and 350 km
326 range in PertD03-Vor are removed for the state variables (the zonal and meridional winds,
327 temperature, specific humidity, and sea-level pressure). Fig. 5 shows that the major initial errors
328 in D02 and D03 for both Typhoons Chan-hom and Maysak are located near the TC eyewall (50–
329 70 km from the typhoon center) (Fig. 5a2–5a4, 5b2–5b4). Another region of higher error
330 magnitude is located near the trough region in the north of the TC environment (Fig. 5a1 and
331 5b1). This indicates the validity of the initial ensemble perturbations that capture the dynamic
332 instabilities of a TC.



333

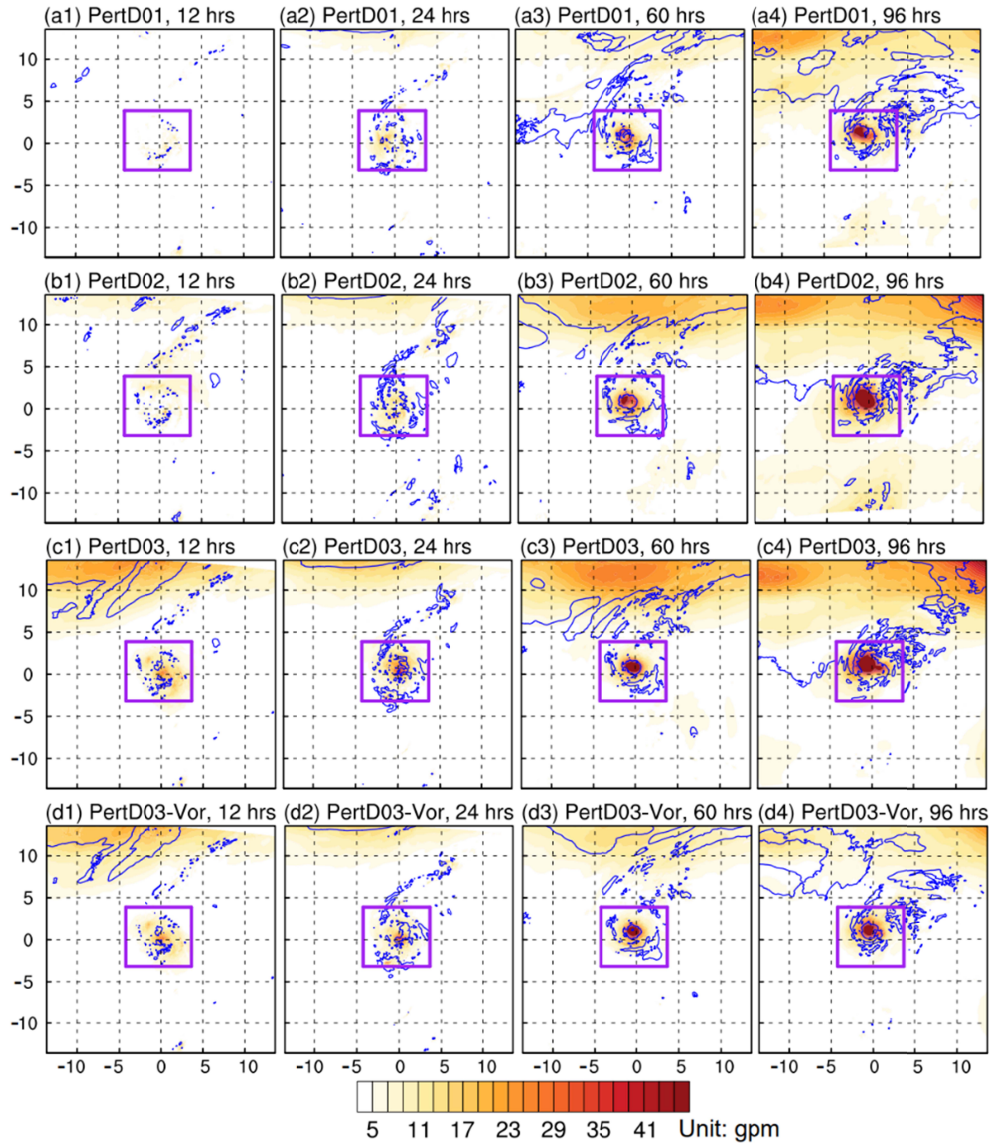
334 Figure 5. Ensemble-averaged initial error amplitudes of the 500-hPa geopotential height in (a1)
 335 D01 of PertD01, (a2) D02 of PertD02, and (a3) D03 of PertD03, and the 500-hPa temperature in
 336 (a4) D03 of PertD03-Vor for Typhoon Chan-hom. (b1)-(b4) are same as (a1)-(a4) but for
 337 Typhoon Maysak.

338

339 In addition to the initial error fields, the ensemble-averaged error growth of the 500 hPa
 340 GH (shaded) and T (contours) in D02 for different experiments is shown in Fig. 6 for Typhoon
 341 Chan-hom and in Fig. 7 for Typhoon Maysak. Domain D03 is highlighted (purple squares) for
 342 reference. Figs. 6a1 and 6b1 show that, even with initial errors in just the environment (i.e.,
 343 PertD01 and PertD02), the errors in the TC inner core (D03) grow rapidly and display a
 344 comparable amplitude to those in the near environment within 12 h. This can be explained by the
 345 more intense error growth of mesoscale convective instabilities in the TC inner core than the
 346 error growth of baroclinic instabilities in the TC environment (Lorenz, 1996; Durran and
 347 Gingrich, 2014; Sun and Zhang, 2016). PertD03 and PertD03-Vor, with initially perturbed D03
 348 present larger errors than PertD01 and PertD02 at 12 h, not only in domain D03 but also in
 349 domain D02 (*cf.* Figs. 6c1, 6d1 and Figs. 6a1, 6b1). This implies that initial errors in the TC
 350 inner core may spread out and lead to forecast uncertainties in the environment of the TC,
 351 probably through their intense interactions with the outer rainbands.

352 The error growth in the TC environment induced by such interactions and the upscale
 353 progression of error growth have a faster rate than the error growth of the environment *per se*
 354 in the first 24 h (*cf.* Fig. 6b2 and 6c2). After this transient period (about 24 h) of upscale error
 355 propagation from the fine-scale TC inner core to the synoptic-scale environment, the initial
 356 errors in the TC environment start to grow and dominate the expansion of forecast uncertainties
 357 in this region. This explains the larger forecast errors in the environment for PertD02 than for
 358 PertD03-Vor from 24 to 96 h (*cf.* Fig. 5b2–b4 and Fig. 5d2–d4). Experiment PertD03 shows the
 359 largest forecast errors in D02 relative to the other experiments for all lead times, especially for
 360 the TC environment. This further suggests the possibility that the particularly strong interaction

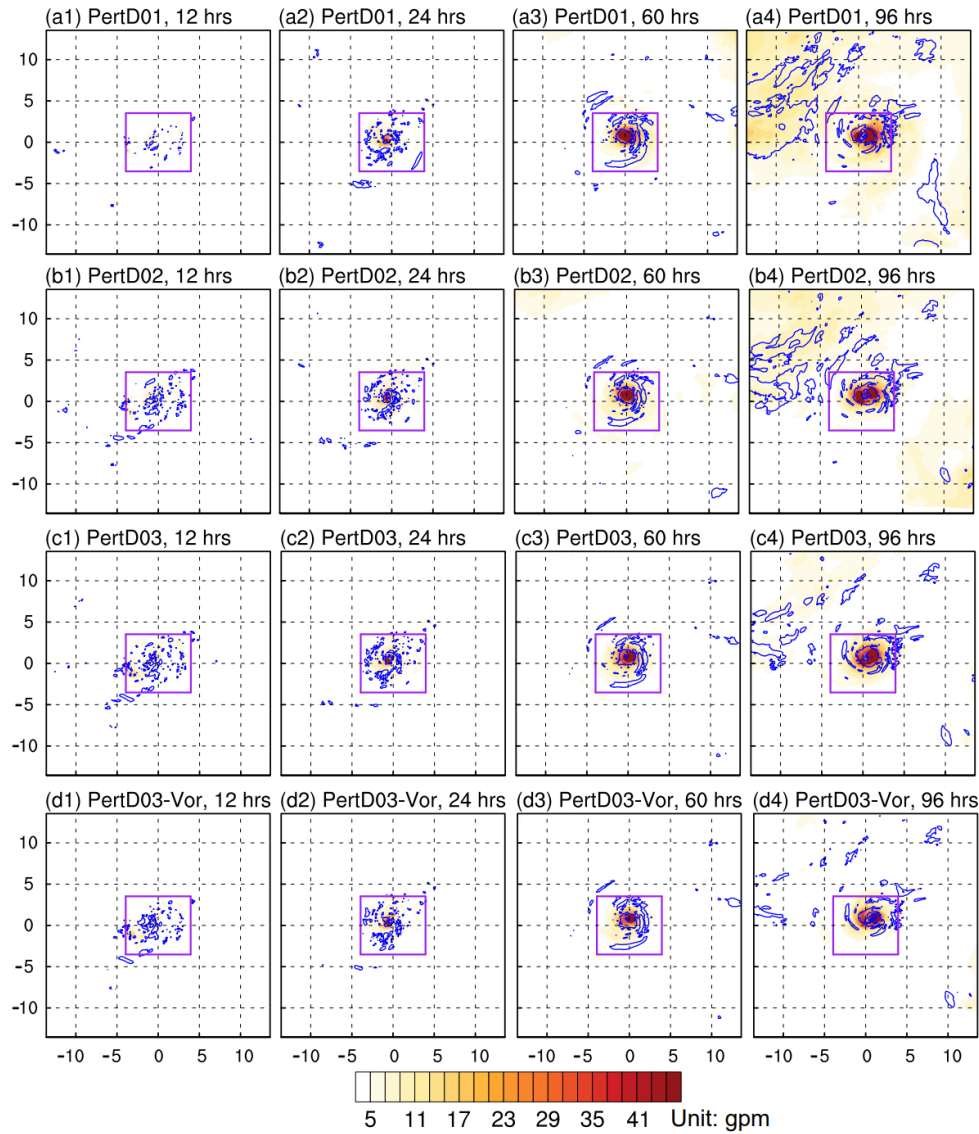
361 between the errors in the inner core and outer rainbands in PertD03 may rapidly produce errors
 362 in the environment of Typhoon Chan-hom. PertD01 presents the smallest overall forecast errors
 363 in D02 throughout all the experiments, which possibly indicates the weak sensitivity of Typhoon
 364 Chan-hom's track to the distant environment beyond about 1300 km. A clearer mechanism for
 365 the different sensitivity behavior of the predictability of TC tracks is warranted in future studies.



366
 367 Figure 6. Ensemble-averaged absolute forecast errors of the 500-hPa GH (shading) and T
 368 (contours) for Typhoon Chan-hom in D02 of (a) PertD01, (b) PertD02, (c) PertD03, and (d)
 369 PertD03-Vor at (a1, b1, c1, d1) 12, (a2, b2, c2, d2) 24, (a3, b3, c3, d3) 60, and (a4, b4, c4, d4) 96
 370 h. Temperature contours are 1, 5, and 9 K. Purple squares show domain D03.

371
 372 Fig. 7 is the same as Fig. 6 but for Typhoon Maysak. It is consistent with Fig. 6 in that
 373 the errors in the TC inner core due to the strong convective instabilities grow much faster than
 374 those in the environment. However, in contrast with Typhoon Chan-hom, the forecast errors in

375 the near environment of Typhoon Maysak are slightly larger in PertD02 and PertD01 than in
 376 PertD03 and PertD03-Vor within the first 24 h (not shown), probably indicating a much weaker
 377 interaction between the inner and outer TC structures relative to Typhoon Chan-hom.
 378 Consequently, the growth of the initial errors in the TC environment plays a more important role
 379 in contributing to its larger forecast errors beyond 24 h compared with the initial errors in the
 380 inner core and outer rainbands of the TC (*cf.* PertD01, PertD02 and PertD03, PertD03-Vor in
 381 Fig. 7).



382
 383 Figure 7. Same as Fig. 6 but for Typhoon Maysak.

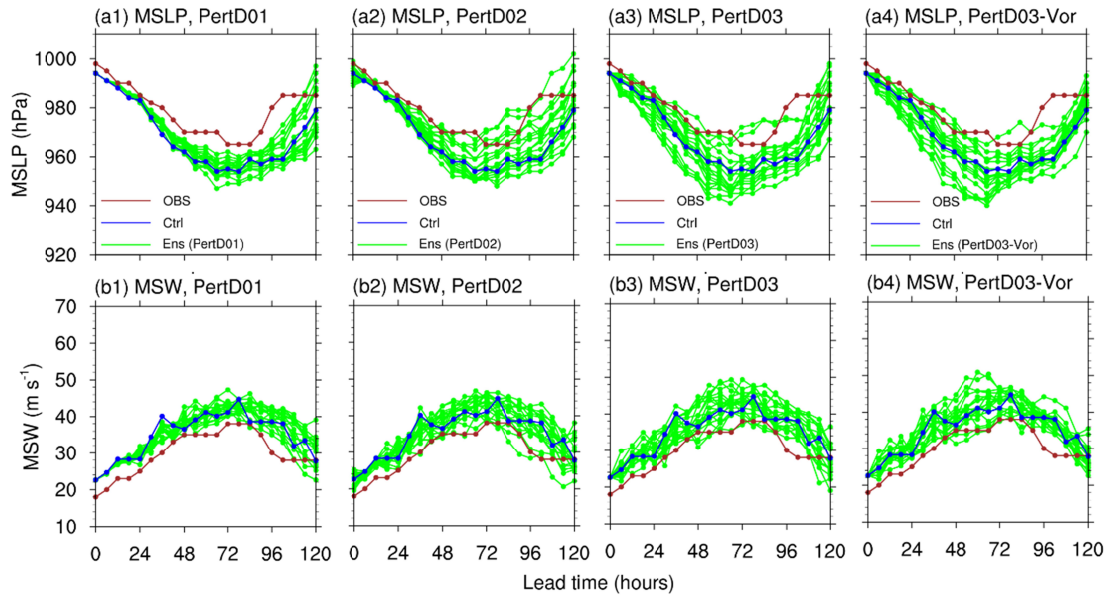
384

385 5 Intrinsic predictability of the TC intensity

386 5.1 Intensity uncertainty

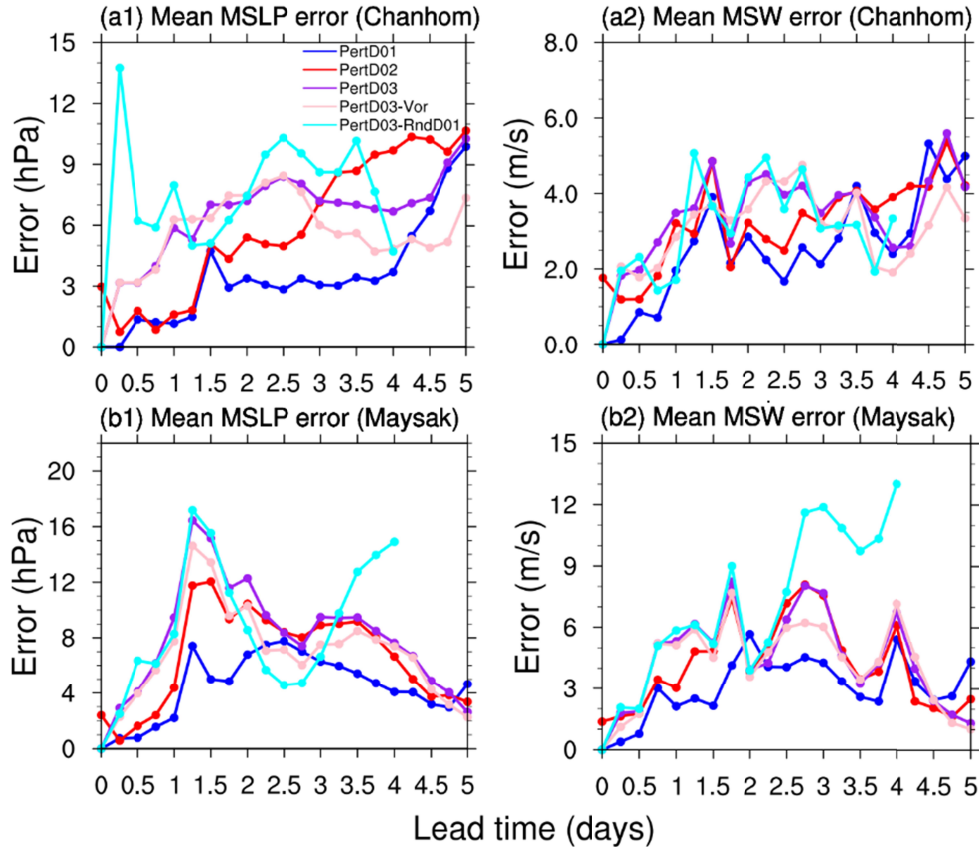
387 This section focuses on the forecast uncertainty for the TC intensity and the relevant error
 388 growth dynamics. The TC intensity is generally measured by two metrics: the minimum sea-

389 level pressure (MSLP) and the MSW. Fig. 8 shows the evolution of the MSLP and MSW in the
 390 ensemble and Ctrl forecasts and observations for Typhoon Chan-hom. The Ctrl forecast errors
 391 compared with the observations averaged over all lead times for Typhoon Chan-hom are about
 392 10 hPa for the MSLP and 6 m s^{-1} for the MSW, which are about half of those for Typhoon
 393 Maysak (not shown). The ensemble intensity spread of Typhoon Chan-hom is also smaller
 394 overall than that of Typhoon Maysak (not shown). The difference in the intensity spread of
 395 Typhoons Chan-hom and Maysak implies that they have distinct intensity predictability. Similar
 396 to the forecasts of the TC ensemble tracks, the ensemble intensities also show different spreads
 397 in experiments PertD01, PertD02, PertD03, and PertD03-Vor for each typhoon (see more details
 398 below).



399
 400 Figure 8. Five-day minimum (a) sea-level pressure (MSLP) and (b) MSW in the Ctrl forecast
 401 (dark blue), observations (brown), and ensemble forecasts (green) of (a1, b1) PertD01, (a2, b2)
 402 PertD02, (a3, b3) PertD03, and (a4, b4) PertD03-Vor for Typhoon Chan-hom.

403
 404 The ensemble-averaged typhoon intensity forecast errors for experiments PertD01,
 405 PertD02, PertD03, and PertD03-Vor in Fig. 8 are calculated and shown in Fig. 9. For both
 406 typhoons, PertD03 (purple) shows larger errors in intensity than PertD01 (blue) and PertD02
 407 (red) in terms of both the MSLP and MSW, especially within the first 2.5 days. The forecast
 408 errors in the intensity of PertD03 remain almost unchanged within the first 2.5 days, even with
 409 the removal of the initial uncertainties in the outer rainband region (*cf.* PertD03 and PertD03-
 410 Vor). These results confirm that the TC intensity is more sensitive to the inner-core structures
 411 within a 250 km radius than to the outer rainbands and environment of the TC. PertD02 (red)
 412 produces larger uncertainties in the TC intensity than PertD01 (dark blue), which indicates that
 413 the predictability of the TC intensity is more sensitive to initial errors in the near environment
 414 than in the far environment.



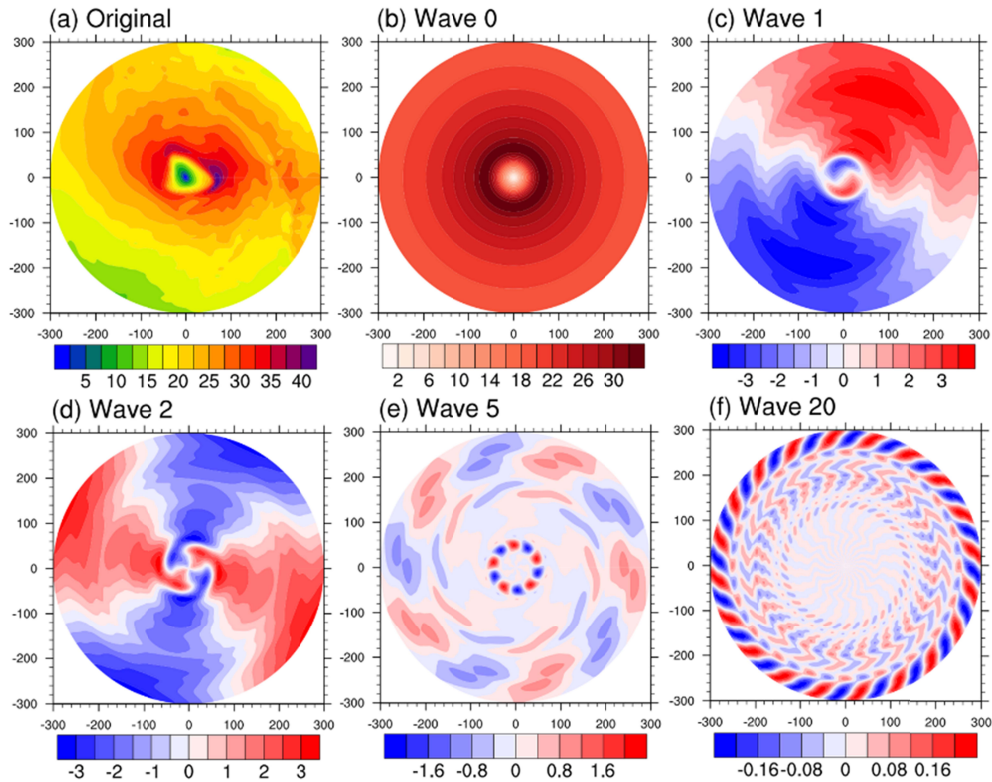
415

416 Figure 9. Intensity errors of the ensemble forecasts against the Ctrl forecast averaged over all
 417 ensemble members in PertD01 (dark blue), PertD02 (red), PertD03 (purple), PertD03-Vor (pink),
 418 and PertD03-RndD01 (cyan) in terms of the (a1, b1) MSLP and (a2, b2) MSW for (a) Typhoon
 419 Chan-hom and (b) Typhoon Maysak.

420

421 5.2 Scale-dependent error growth

422 Previous studies have shown that the TC intensity evolution is closely related to both the
 423 symmetrical and asymmetrical structures of the inner core (Moller and Montgomery, 2000;
 424 Nolan et al., 2007; Yang et al., 2007; Persing et al., 2013). To determine how the initial errors
 425 inherent in the TC influence the predictability of intensity, we used a Fourier decomposition
 426 algorithm to decompose the azimuthal structures of the 10-m wind amplitude field within a 300-
 427 km radius of the TC center, as in Judt et al. (2016). The original 10-m wind amplitude field
 428 within the 300-km radius can be decomposed into the mean state (i.e., wave number 0) and 180
 429 wave component fields (Fig. 10). Following the classification of Judt et al. (2016), wave number
 430 0 represents the mean vortex and wave number 1 is the vortex-scale asymmetry. The structure of
 431 wave numbers 2–5 resembles the TC rain bands and the remaining scales ≥ 6 are associated with
 432 smaller mesoscale and convective features in the TC circulation.

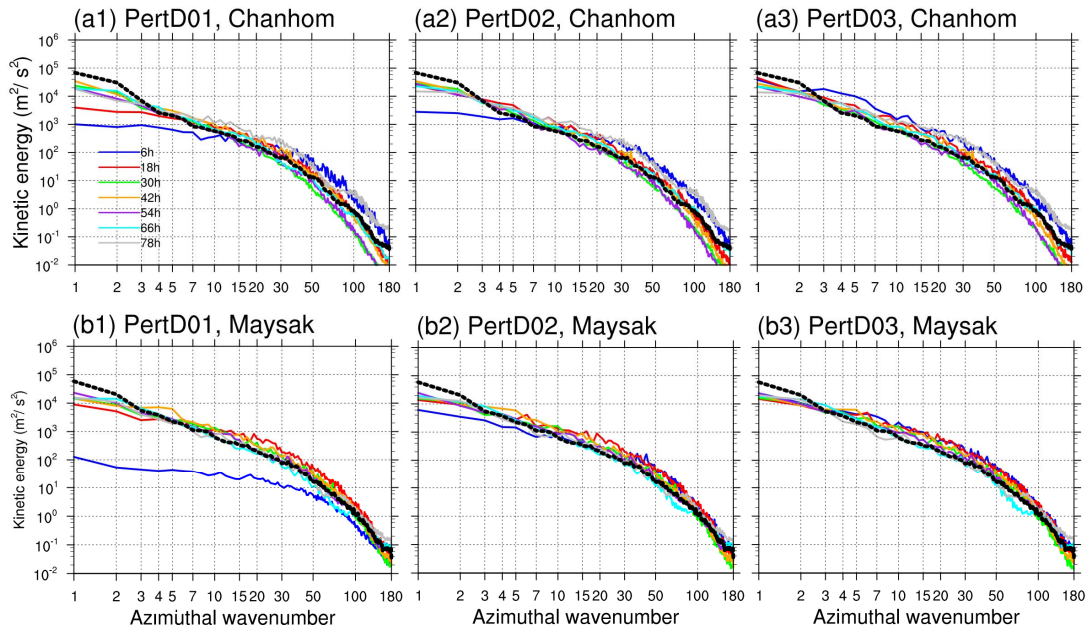


433
 434 Figure 10. (a) 10-m wind speed (m s^{-1}) in a 300-km radius from the TC center in the 2.25-day
 435 Ctrl forecast of Typhoon Chan-hom and its azimuthally decomposed components at wave
 436 numbers (b) 0, (c) 1, (d) 2, (e) 5, and (f) 20.

437

438 Fig. 11 shows the azimuthal mean error variances of the 10-m wind amplitude at different
 439 scales in ensembles integrated over the TC inherent region (a 300-km radius from the center) as a
 440 function of the lead time for PertD01, PertD02, and PertD03 of Typhoons Chan-hom and
 441 Maysak. The temporal mean variability of the 10-m wind amplitude of the Ctrl experiment in the
 442 same region (black dashed lines) is shown as a reference. The time points at which the error
 443 variance exceeds the reference are regarded as the predictability limit at that scale. It is
 444 noticeable that for both Typhoons Chan-hom and Maysak the mesoscale and convective scales
 445 (wave numbers ≥ 6) can only be predicted up to 6 h if the initial errors are superposed in the near
 446 (i.e., PertD02) or TC inner-core (i.e., PertD03) regions (see Fig. 11a2, 11a3, 11b2, and 11b3). If
 447 only the far environment is perturbed (i.e., PertD01), then the predictability limit of these scales
 448 can be slightly extended to 12–18 h (Fig. 11a1 and 11b1). In contrast with the conclusion of Judt
 449 et al. (2016) that the rainbands are predictable within a few days, we found that the rainband
 450 scales at wave numbers 3–5 can only be predicted within the first 18 h regardless of the regions
 451 of the initial errors. These different results possibly indicate that the initial uncertainties may
 452 degrade the prediction performance of the rainband-scale features more severely at earlier lead
 453 times than the model uncertainties. It could also mean that the two typhoon cases analyzed in this
 454 study have lower predictability than Hurricane Earl, which was the subject of the study in Judt et
 455 al. 2016. On the other hand, our results are consistent with the results of Judt et al. (2016) in that
 456 the mean flow of the TC (wave number 0; not shown) and the major asymmetrical components

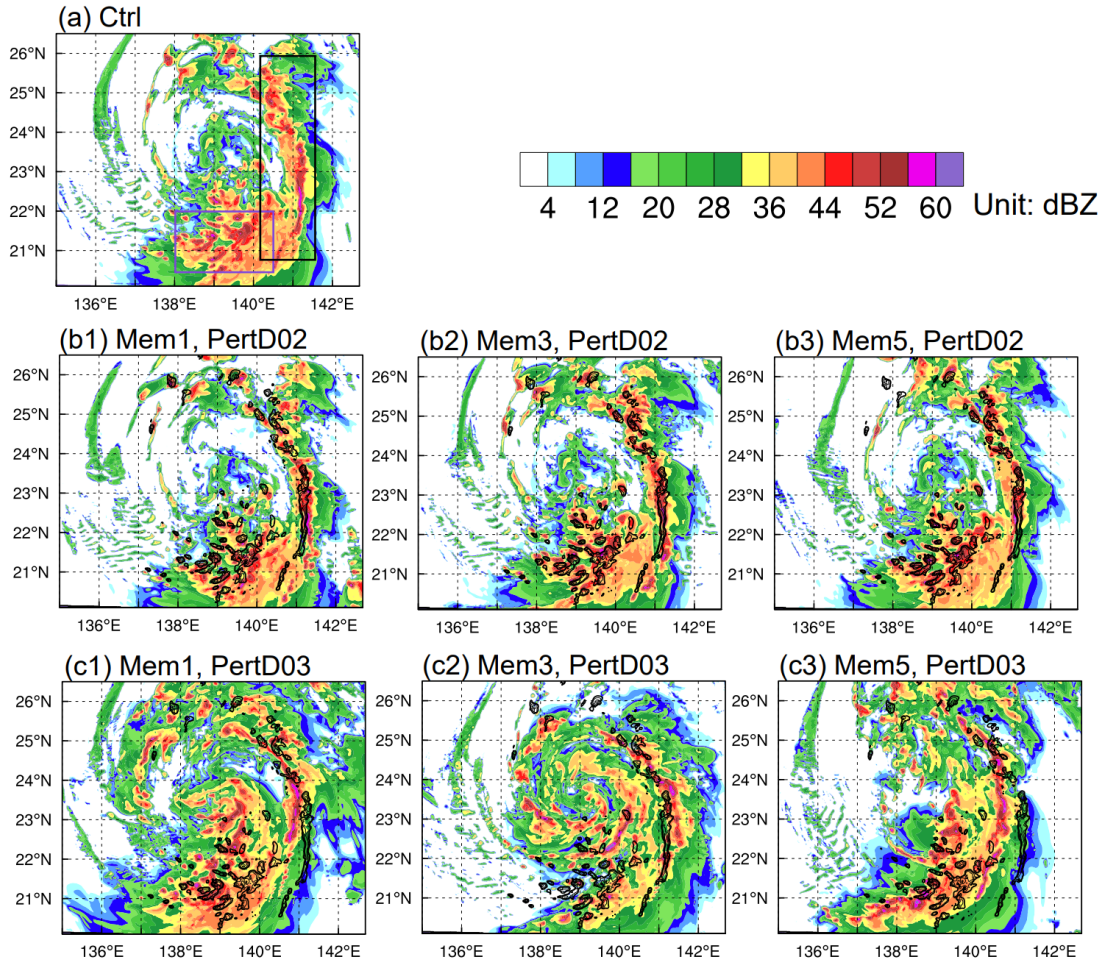
457 (wave numbers 1–2) are resistant to the upscale error propagation from smaller scales and remain
 458 predictable for a much longer time of at least 3.5 days.



459
 460 Figure 11. Azimuthally mean and regionally integrated (0–300 km) error variances ($\text{m}^2 \text{s}^{-2}$) at
 461 different scales of the 10-m wind amplitude averaged over all ensemble members at different
 462 lead times for (a1, b1) PertD01, (a2, b2) PertD02, and (a3, b3) PertD03 of (a) Typhoon Chan-
 463 hom and (b) Typhoon Maysak.

464

465 As shown in Fig. 11a2 and 11a3, the rainband scales of wave numbers 3–5 for Typhoon
 466 Chan-hom are still predictable at 6 h in PertD02 but are almost unpredictable at 6 h in PertD03.
 467 We therefore also show the 6-h composite radar reflectivity in D03, which roughly reflects the
 468 TC-induced rainfall in the Ctrl and ensemble forecasts of PertD02 and PertD03 (Fig. 12). Only
 469 three arbitrarily selected members are shown. Fig. 12a shows a clear spiral rainfall structure in
 470 the Ctrl experiment, extended from the south to the east and northeast of Typhoon Chan-hom,
 471 with most regions >30 dBZ. The southern rainfall conglomeration (highlighted with a purple
 472 rectangle in Fig. 12a) is organized as a cluster of convective storms and the eastern rainfall
 473 conglomeration (highlighted with a black rectangle in Fig. 12a) is characterized by a narrow,
 474 north–south stretched rainband. Noticeably, the members in PertD02 with initial perturbations in
 475 the near environment capture the placement and structure of the eastern rainband and the
 476 convective rainfall at 6 h (*cf.* shaded and black contours). However, the members in PertD03
 477 with initial perturbations in the TC inner core present poor skill in predicting the long rainband in
 478 the east, with significant errors in both position and strength. In addition, the convective storms
 479 in the south of Typhoon Chan-hom in the ensembles of PertD03 are almost randomly distributed
 480 or completely displaced compared with those in the Ctrl experiment. The comparison indicates
 481 that the initial errors in the TC inner core can intensively constrain the predictability limit of the
 482 TC rainbands to <6 h.



483

484 Figure 12. Composite radar reflectivity (shaded) in D03 of in the 6-h (a) Ctrl and (b1–b3)
 485 ensemble forecasts of PertD02 and (c1–c3) PertD03. The composite radar reflectivity (≥ 44 dBZ)
 486 of the Ctrl experiment is shown as black contours in (b1–b3) and (c1–c3) for comparison.

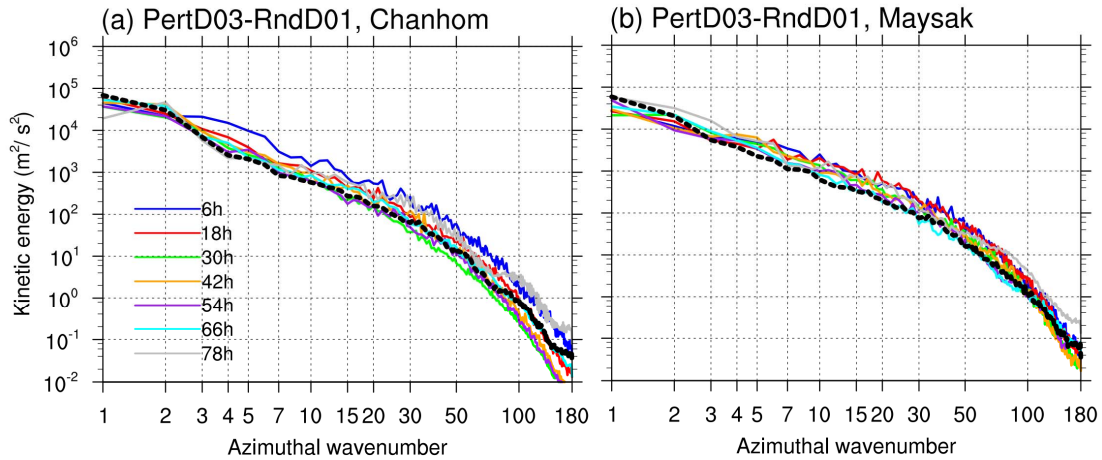
487

488 5.3 Source of predictability in the TC intensity

489 Fig. 11 shows that wave numbers 0–2 of the 10-m wind amplitude are resilient to the
 490 upscale error growth, in contrast with the fast growth and saturation of the errors at smaller
 491 scales. To understand the source of the predictability of the low wavenumber components, a
 492 supplementary experiment (hereafter called PertD03-RndD01) was carried out. This experiment
 493 was similar to PertD03 but additionally replaced the initial conditions of D01 in the ensemble
 494 forecasts with the variable fields downscaled from the GFS analysis at another valid time. In
 495 PertD03-RndD01, D01 for both Typhoons Chan-hom and Maysak uses the downscaled analysis
 496 at 0000 UTC on 18 August 2020, which is nearly two months and ten days, respectively, from
 497 the initial times of the experiment.

498 Fig. 13 shows the temporal evolution of the wave spectrum of the surface wind of the TC
 499 inner core for experiment PertD03-RndD01. Wave numbers ≥ 2 become saturated in < 6 h, the
 500 same as in PertD03 (see Fig. 12). However, the error variances of wave numbers 1–2 become

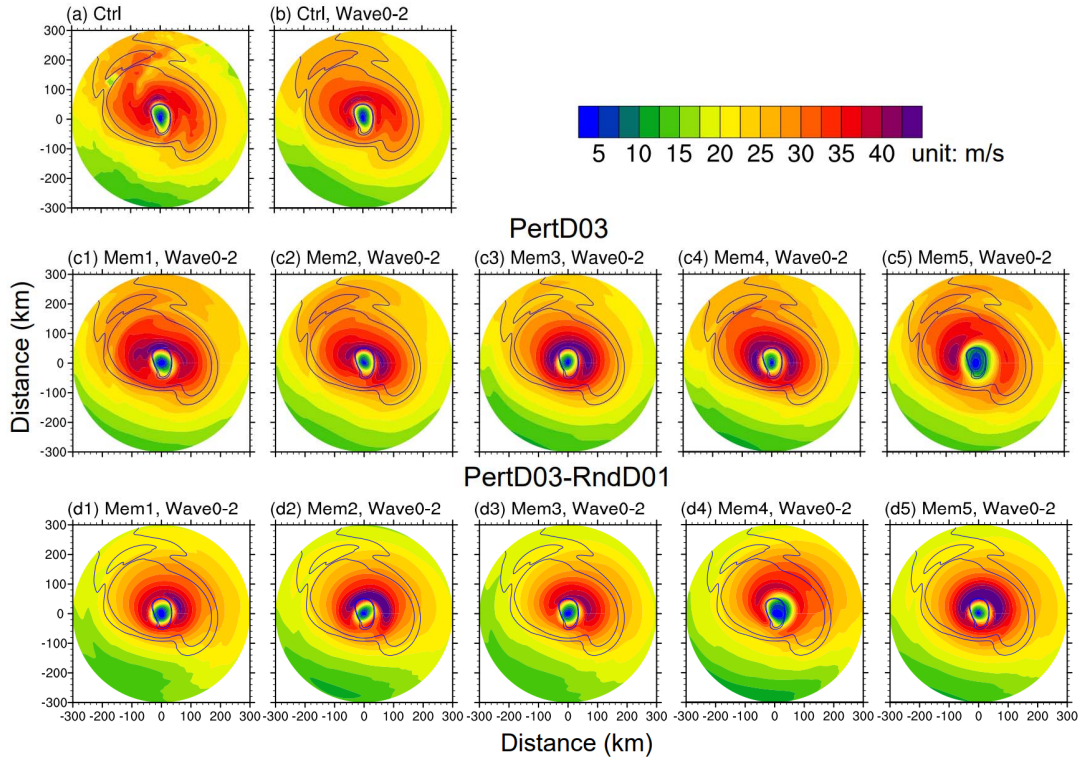
501 nearly saturated within about one day, in contrast with those in PertD03 (see Fig. 12), which
 502 remain predictable at 3.5 days. This result indicates that the major source of the predictability of
 503 the surface wind components at wave numbers 1–2 is the synoptic-scale environment of the TC,
 504 which is consistent with the conclusions of Judt et al. (2016). The error variance of the mean
 505 vortex flow (i.e., wave number 0) is still significantly smaller than the saturation value, even
 506 with a nearly chaotic environmental field (not shown), implying that the TC mean vortex may be
 507 efficiently predicted for a fairly long time.



508
 509 Figure 13. Same as Fig. 11 but for PertD03-RndD01 of (a) Typhoon Chan-hom and (b) Typhoon
 510 Maysak.

511
 512 Fig. 14 shows the original 10-m wind speed field in the 300-km radius of the Ctrl
 513 experiment for Typhoon Chan-hom at 66 h and its composite wind field for wave numbers 0–2
 514 (Fig. 14a and 14b). The composite surface wind of wave numbers 0–2 in the PertD03 and
 515 PertD03-RndD01 ensembles are also shown for comparison (Fig. 14c1–c5 and 14d1–d5,
 516 respectively). Wave components 0–2 can explain almost 95% of the variance of the 10-m wind
 517 amplitude in the Ctrl experiment (*cf.* Fig. 14a and 14b). When comparing the ensemble members
 518 of PertD03 and PertD03-RndD01, the formers can roughly capture the composite surface wind
 519 structure of wave numbers 0–2 in the Ctrl experiment (*cf.* shading and contours) with a mean
 520 spatial correlation of 0.94, which is much better than the latter of 0.83. This result is consistent
 521 with the lower error variance at wave numbers 0–2 in PertD03 than in PertD03-RndD01 (*cf.* Figs
 522 11a3 and 13a).

523 Although the composite surface wind amplitude of waves 0–2 in PertD03 has a longer
 524 predictability limit than that in PertD03-RndD01 (at least 3.5 days versus almost one day),
 525 PertD03 shows a similar performance to PertD03-RndD01 in terms of the MSLP and MSW for
 526 both typhoons (*cf.* Fig. 9, cyan and purple curves), except for the MSLP of Typhoon Chan-hom.
 527 This suggests that the MSW has limitations as a metric to measure TC intensity (Vukicevic et al.,
 528 2014; Judt et al., 2016). The MSW defines the 10-m maximum wind speed at a certain time and
 529 point, which is not only related to wave numbers 0–2 but also has contribution from the highly
 530 turbulent, rapidly evolving asymmetrical wind field in TCs that has very low predictability.

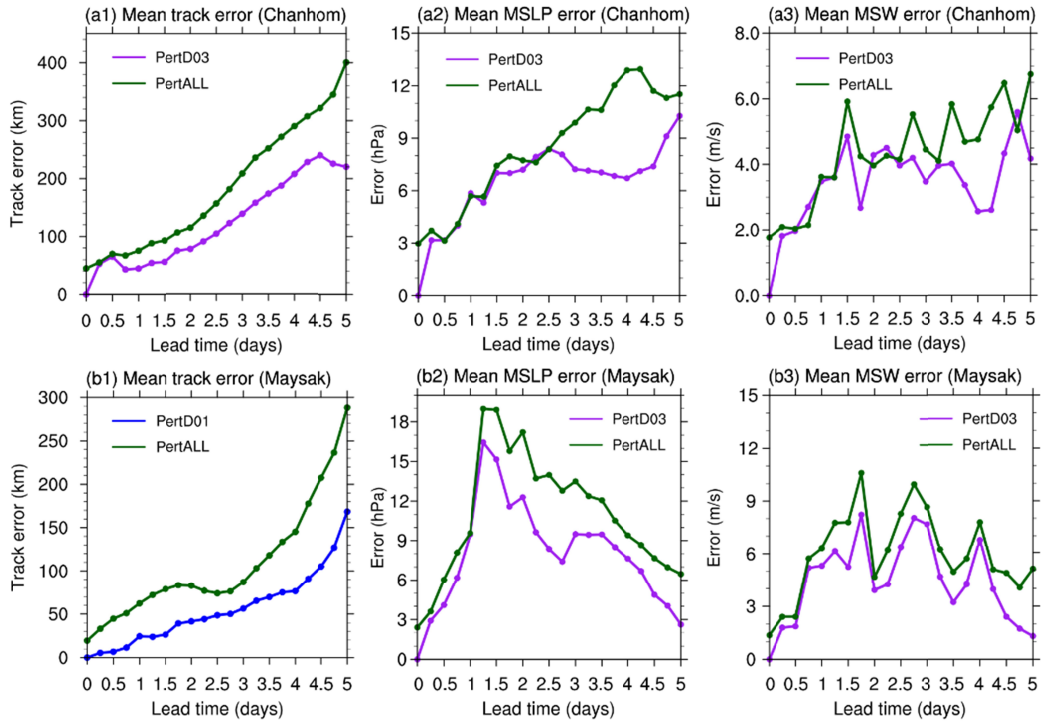


531
 532 Figure 14. (a) 10-m wind speed forecast (shading) in the 300-km radius of the Ctrl experiment at
 533 66 h for Typhoon Chan-hom and (b) its composite wind field (shading) of wave numbers 0–2.
 534 (c1–c5) Composite 10-m wind speed fields (shading) of wave numbers 0–2 of the ensemble
 535 forecasts for PertD03 at 66 h. (d1–d5) are same as (c1)–(c5) but for PertD03-RndD01 at 66 h.
 536 Blue contours highlight wind speeds of 25 and 27.5 m s⁻¹ in the composite wind field of the Ctrl
 537 experiment in part (b).

538

539 6 Combined effects of initial and lateral boundary perturbations on the TC predictability

540 For practical predictions of TCs, uncertainties exist in not only the initial conditions but
 541 also the boundary conditions. This section considers the combined effects of the initial
 542 perturbations in all three nested domains and the boundary perturbations (i.e., PertALL) on the
 543 TC track and intensity predictability. Fig. 15 compares the ensemble-averaged errors in the TC
 544 track and intensity errors between PertALL and the worst-performing experiment (i.e., the
 545 largest forecast error) among PertD01, PertD02, and PertD03. These are PertD03 for the track
 546 and intensity of Typhoon Chan-hom and PertD01 for the track and PertD03 for the intensity of
 547 Typhoon Maysak (see Figs 4 and 9). The comparison in Fig. 15 shows that PertALL has larger
 548 forecast errors in both the track and intensity than the experiments with initial errors in particular
 549 regions for both Typhoons Chan-hom and Maysak. This means that the track and intensity of the
 550 TC become more unpredictable when taking into account all the sources of uncertainties in the
 551 initial and boundary conditions.

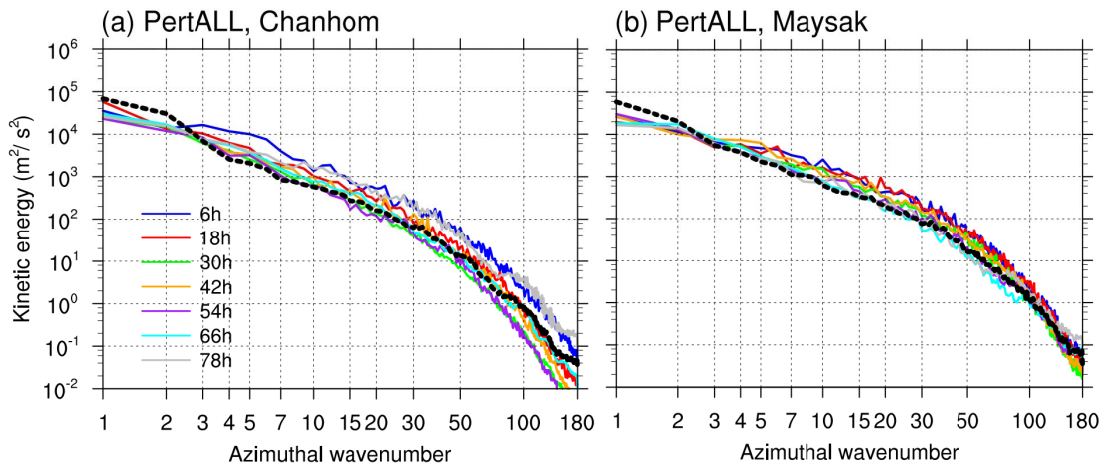


552

553 Figure 15. Ensemble-averaged forecast errors of the (a1, b1) track, (a2, b2) MSLP, and (a3, b3)
 554 MSW for PertALL (dark green) and PertD03 (purple) of (a) Typhoon Chan-hom and (b)
 555 Typhoon Maysak. In Fig. 15b1, PertALL is compared with PertD01 because the latter has the
 556 worst performance in all other experiments.

557

558 Fig. 16 shows the ensemble-averaged error variance spectrum of the 10-m wind
 559 amplitude in the TC inner core of PertALL. The temporal evolution of the error spectrum in
 560 PertALL is similar to that in PertD03, although PertALL has larger forecast errors in the MSW
 561 than PertD03 (see Fig. 15). The wind components of wave numbers 0–2 remain predictable for
 562 about three days, which shows that the scales of wave numbers 0–2, which inherit their
 563 predictability from the TC environment, are the major source that facilitates a skillful prediction
 564 of TC intensity up to a few days.



565

566 Figure 16. Same as Fig. 13 but for PertALL.

567

568 **7 Conclusions and discussion**

569 Gaining a profound comprehension of the intrinsic predictability of TCs is vital for
570 enhancing the accuracy of their track and intensity forecasts. The concept of intrinsic
571 predictability centers on how initial errors amplify and impact the prediction outcome when an
572 almost perfect procedure is employed. This can offer a rough estimate of the upper limit of the
573 predictive skill and the predictability threshold. To examine the intrinsic predictability of TC
574 track and intensity, we compared convection-resolving control forecasts and ensemble forecasts
575 with perturbed initial conditions using a regional HWRF model. Our primary objective was to
576 investigate the sensitivity of TC track and intensity uncertainties to initial errors in various
577 regions and the corresponding error growth dynamics. A model configuration with three two-
578 way nested domains (18/6/2 km resolution) was used to provide a relatively realistic simulation
579 of the scales and characteristics of the inner core and environment of TCs. Experiments were
580 designed to investigate the influence of the initial errors in (1) the far environment (1300–3500
581 km from the TC center), (2) the near environment (350–1300 km), and (3) TC inner core and
582 outer rainband regions (0–350 km) on the predictability of the track and intensity. We selected
583 two typhoons, Chan-hom and Maysak, that occurred in the western North Pacific Ocean in 2020
584 and distinct uncertainty in both track and intensity to demonstrate the case-specific nature of
585 predictability analysis. Our main results are summarized here.

586 (1) The most sensitive region of the initial errors that affect the TC track uncertainties is
587 case-dependent. For a case with remarkably large track errors (e.g., Typhoon Chan-hom), the
588 most sensitive region of the initial errors is the combined region of the TC inner core and outer
589 rainbands (0–350 km). The strong interaction of the initial errors in the TC inner core and outer
590 rainbands may lead to increased uncertainties in the TC environment that degrade the track
591 forecast performance (Fig. 6). The track uncertainties with initial errors in the combined area of
592 the TC inner core and outer rainbands are nearly double those with initial errors in either region
593 (Fig. 4a).

594 (2) By contrast, for a case (e.g., Typhoon Maysak) with a much more predictable track, the
595 most sensitive region of initial errors is the near environment (350–1300 km) in the early stages
596 (about 2.5 days) and then the far environment (1300–3500 km; Fig. 4b) in the later stages. In this
597 case, the growth of the initial errors in the environment is dominant in the track forecast as a
598 result of the weak interactions between the TC inner and outer structures (Fig. 7).

599 (3) The most sensitive region of the initial errors for uncertainties in intensity is the inner
600 core region (0–250 km) for both cases. Our results emphasize that not only the scale of the initial
601 or model perturbations but also the regions of these perturbations, matter in the predictability of
602 the TC intensity and track.

603 (4) Our results are consistent with the conclusions of Judt (2016) that the errors at meso- and
604 convective scales (wave numbers ≥ 6) of the TC inner core grow rapidly and saturate within 6–12
605 h, regardless of the regions of the initial errors. However, we found the rainband scales at wave
606 numbers 3–5 can only be predicted up to 18 h regardless of the regions of the initial errors, rather

607 than the few days of Judt (2016). This suggests the initial errors could possibly constrain the
608 predictability of the features at the rainband scale more severely than the model errors.

609 (5) The mean vortex and asymmetrical structures of the TC at wave numbers 1–2 remain
610 predictable for at least 3.5 days because their predictability source is the synoptic-scale
611 environmental flow. Nevertheless, a more accurate environmental flow may not guarantee an
612 improved prediction of the MSLP and MSW because these two instantaneous metrics are also
613 influenced by highly turbulent and rapidly evolving finer-scale features that have very short
614 predictability.

615 Although the influences of the region-dependent initial errors on uncertainties in the TC
616 track and intensity were analyzed and compared and the most sensitive regions identified in this
617 study, we still do not know the precise mechanisms of how the initial errors in different regions
618 induce uncertainties in TC track and intensity. For Typhoon Chan-hom with significant track
619 errors, how do the initial errors in the TC inner core and outer rainbands intensively interact and
620 influence the TC environment and track? Why are the interactions between the inner and outer
621 structures of Typhoon Maysak significantly weaker than those of Typhoon Chan-hom? Which
622 physical processes in the TC inner core cause the remarkable intensity uncertainties of Typhoons
623 Chan-hom and Maysak? These questions remain unclear and need further exploration in future
624 studies.

625

626

627 **Acknowledgments**

628 The authors are grateful to Drs. Yuntao Wei and Guokun Dai at Fudan University, Dr. Deming
629 Meng at Nanjing University, Prof. Tao Lian at the Second Institute of Oceanography, Profs.
630 Wenjun Zhang, Xiefei Zhi, Qingqing Li, and Chao Wang at Nanjing University of Information
631 Science and Technology in China for their input and helpful discussions. This study was
632 supported by the National Natural Science Foundation of China (Grant No. 42288101 and
633 42105054).

634

635 **Open Research**

636 The global ensemble forecast product of GEFS at NCEP is downloaded from NCEP operational
637 product inventory at <https://www.nco.ncep.noaa.gov/pmb/products/gens/>. The forecast product
638 of the global forecast system (GFS) at NCEP is downloaded from
639 <https://rda.ucar.edu/datasets/ds084.1/>. The Typhoon best-track data can be downloaded from the
640 data archive center at <https://ncics.org/ibtracs/index.php?name=YearBasin-2020>

641

642

643

644 **References**

- 645 Anwender, D., Harr, P. A., and Jones, S. C. (2008). Predictability associated with the
 646 downstream impacts of the extratropical transition of tropical cyclones: Case studies. *Mon. Wea.*
 647 *Rev.*, *136*, 3226–3247, doi:10.1175/2008MWR2249.1.
- 648
 649 Ashcroft, J., Schwendike, J., Griffiths, S. D., Ross, A. N., & Short, C. J. (2021). The impact of
 650 weak environmental steering flow on tropical cyclone track predictability. *Quarterly Journal of*
 651 *the Royal Meteorological Society*, *147*(741), 4122–4142. <https://doi.org/10.1002/qj.4171>
- 652
 653 Black, M. L., Gamache, J. F., Marks, J. D., Samsury, C. E., & Willoughby, H. E. (2002). Eastern
 654 pacific Hurricanes Jimena of 1991 and Olivia of 1994: The effect of vertical shear on structure
 655 and intensity. *Monthly Weather Review*, *130*(9), 2291–2312. [https://doi.org/10.1175/1520-0493\(2002\)130<2291:EPHJOA>2.0.CO;2](https://doi.org/10.1175/1520-0493(2002)130<2291:EPHJOA>2.0.CO;2)
- 656
 657
 658 Cangialosi JP, Franklin JL. 2014. ‘National Hurricane Center forecast verification
 659 report’. http://www.nhc.noaa.gov/verification/pdfs/Verification_2013.pdf
- 660
 661 Chen, S. S., Knaff, J. A., & Marks, F. D. (2006). Effects of vertical wind shear and storm motion
 662 on tropical cyclone rainfall asymmetries deduced from TRMM. *Monthly Weather*
 663 *Review*, *134*(11), 3190–3208. <https://doi.org/10.1175/MWR3245.1>
- 664
 665 Chen, S. S., Price, J. F., Zhao, W., Donelan, M. A., & Walsh, E. J. (2007). The CBLAST-
 666 Hurricane program and the next-generation fully coupled atmosphere-wave-ocean models for
 667 hurricane research and prediction. *Bulletin of the American Meteorological Society*, *88*(3), 311–
 668 317. <https://doi.org/10.1175/BAMS-88-3-311>
- 669
 670 Chen, S. S., Zhao, W., Donelan, M. A., & Tolman, H. L. (2013). Directional wind-wave
 671 coupling in fully coupled atmosphere-wave-ocean models: Results from CBLAST-
 672 hurricane. *Journal of the Atmospheric Sciences*, *70*(10), 3198–3215. <https://doi.org/10.1175/JAS-D-12-0157.1>
- 673
 674
 675 Chia, H. H., and Ropelewski, C. F. (2002). The interannual variability in the genesis location of
 676 tropical cyclones in the northwest Pacific. *Journal of Climate*, *15*(20), 2934–2944.
 677 [https://doi.org/10.1175/1520-0442\(2002\)015<2934:TIVITG>2.0.CO;2](https://doi.org/10.1175/1520-0442(2002)015<2934:TIVITG>2.0.CO;2)
- 678
 679 DeMaria, M., Sampson C. R., Knaff, J. A., and Musgrave, K. D., (2014). Is tropical cyclone
 680 intensity guidance improving? *Bull. Amer. Meteor. Soc.*, *95*, 387–398, doi:10.1175/BAMS-D-12-00240.1.
- 681
 682
 683 Durran, D., and Gingrich M., (2014). Atmospheric predictability: Why butterflies are not of
 684 practical importance. *J. Atmos. Sci.*, *71*, 2476–2488, doi:10.1175/JAS-D-14-0007.1.
- 685
 686 Emanuel, K. A. (1986). An air-sea interaction theory for tropical cyclones. Part I: steady-state
 687 maintenance. *Journal of the Atmospheric Sciences*, *43*(6), 585–604.
 688 [https://doi.org/10.1175/1520-0469\(1986\)043<0585:aasitf>2.0.co;2](https://doi.org/10.1175/1520-0469(1986)043<0585:aasitf>2.0.co;2)

- 689
690 Emanuel, K., DesAutels, C., Holloway, C., & Korty, R. (2004). Environmental control of
691 tropical cyclone intensity. *Journal of the Atmospheric Sciences*, *61*(7), 843–858.
692 [https://doi.org/10.1175/1520-0469\(2004\)061<0843:ECOTCI>2.0.CO;2](https://doi.org/10.1175/1520-0469(2004)061<0843:ECOTCI>2.0.CO;2)
693
- 694 Feng, J. and Wang, X. G., (2019). Impact of assimilating upper-level dropsonde observations
695 collected during the TCI field campaign on the prediction of intensity and structure of Hurricane
696 Patricia (2015), *Mon. Wea. Rev.*, *147*, 3069–3089.
697
- 698 Feng, J. and Wang, X. G., (2021). Impact of increasing horizontal and vertical resolution of the
699 hurricane WRF model on the analysis and prediction of Hurricane Patricia (2015). *Mon. Wea.*
700 *Rev.*, *149*(2), 419–441. DOI: 10.1175/MWR-D-20-0144.1
701
- 702 Feng, J., Qin, X., Wu, C., Zhang, P., Yang, L., Shen, X. S., Han, W., Liu, Y. Z., (2022)
703 Improving typhoon predictions by assimilating the retrieval of atmospheric temperature profiles
704 from the FengYun-4A's Geostationary Interferometric Infrared Sounder (GIIRS), *Atmospheric*
705 *Research*, *280*, 106391, ISSN 0169-8095, <https://doi.org/10.1016/j.atmosres.2022.106391>.
706
- 707 Ferrier, B. S., (1994). A double-moment multiple-phase four-class bulk ice scheme. Part I:
708 Description. *J. Atmos. Sci.*, *51*, 249–280, [https://doi.org/10.1175/1520-](https://doi.org/10.1175/1520-0469(1994)051<0249:ADMMPF>2.0.CO;2)
709 [0469\(1994\)051<0249:ADMMPF>2.0.CO;2](https://doi.org/10.1175/1520-0469(1994)051<0249:ADMMPF>2.0.CO;2).
710
- 711 Ferrier, B. S., (2005). An efficient mixed-phase cloud and precipitation scheme for use in
712 operational NWP models. *2005 Spring Meeting*, San Francisco, CA, Amer. Geophys. Union,
713 Abstract A42A-02.
714
- 715 Finocchio, P. M., & Majumdar, S. J. (2017). The Predictability of Idealized Tropical Cyclones in
716 Environments With Time-Varying Vertical Wind Shear. *Journal of Advances in Modeling Earth*
717 *Systems*, *9*(8), 2836–2862. <https://doi.org/10.1002/2017MS001168>
718
- 719 Gopalakrishnan, S. G., Marks, F., Zhang, X., Bao, J. W., Yeh, K. S., & Atlas, R. (2011). The
720 experimental HWRF system: A study on the influence of horizontal resolution on the structure
721 and intensity changes in tropical cyclones using an idealized framework. *Monthly Weather*
722 *Review*, *139*(6), 1762–1784. <https://doi.org/10.1175/2010MWR3535.1>
723
- 724 Hakim, G. J. (2013). The variability and predictability of axisymmetric hurricanes in statistical
725 equilibrium. *Journal of the Atmospheric Sciences*, *70*(4), 993–1005. [https://doi.org/10.1175/JAS-](https://doi.org/10.1175/JAS-D-12-0188.1)
726 [D-12-0188.1](https://doi.org/10.1175/JAS-D-12-0188.1)
727
- 728 Han, J., and Pan, H.-L., (2006). Sensitivity of hurricane intensity forecasts to convective
729 momentum transport parameterization. *Mon. Wea. Rev.*, *134*, 664–
730 674, <https://doi.org/10.1175/MWR3090.1>.
731
- 732 Hong, S.-Y., and Pan, H.-L., (1996). Nonlocal boundary layer vertical diffusion in a medium-
733 range forecast model. *Mon. Wea. Rev.*, *124*, 2322–
734 2339, [https://doi.org/10.1175/15200493\(1996\)124<2322:NBLVDI>2.0.CO;2](https://doi.org/10.1175/15200493(1996)124<2322:NBLVDI>2.0.CO;2).

- 735
736 Houze, R. A. (2010, February). Clouds in tropical cyclones. *Monthly Weather Review*.
737 <https://doi.org/10.1175/2009MWR2989.1>
738
- 739 Harr, P. A., Anwender, D., and Jones, S. C., (2008). Predictability associated with the
740 downstream impacts of the extratropical transition of tropical cyclones: Methodology and a case
741 study of Typhoon Nabi (2005). *Mon. Wea. Rev.*, *136*, 3205–3225,
742 doi:10.1175/2008MWR2248.1.
743
- 744 Hazelton, A., Alaka Jr, G. J., Fischer, M. S., Torn, R., & Gopalakrishnan, S. (2023). Factors
745 Influencing the Track of Hurricane Dorian (2019) in the West Atlantic: Analysis of a HAFS
746 Ensemble. *Monthly Weather Review*, *151*(1), 175–192
747
- 748 Holland, G. J. (Ed.) (1993), Tropical cyclone motion, in *Global Guide to Tropical Cyclone*
749 *Forecasting*, Tech. Doc. WMO/TD 560, Trop. Cyclone Programme Rep. TCP-31, chap. 3, World
750 Meteorol. Org., Geneva, Switzerland. (Available
751 at http://www.bom.gov.au/bmrc/pubs/tcguide/ch3/ch3_tableo
752
- 753 Houze, R. A., Chen, S. S., Lee, W.-C., Rogers, R. F., Moore, J. A., Stossmeister, G. J., ...
754 Brodzik, S. R. (2006). The Hurricane Rainband and Intensity Change Experiment: Observations
755 and Modeling of Hurricanes Katrina, Ophelia, and Rita. *Bulletin of the American Meteorological*
756 *Society*, *87*(11), 1503–1522. <https://doi.org/10.1175/bams-87-11-1503>
757
- 758 Ito, K., & Wu, C. C. (2013). Typhoon-position-oriented sensitivity analysis. part I: Theory and
759 verification. *Journal of the Atmospheric Sciences*, *70*(8), 2525–2546.
760 <https://doi.org/10.1175/JAS-D-12-0301.1>
761
- 762 Judt, F., and S. S. Chen, 2010: Convectively generated potential vorticity in rainbands and
763 formation of the secondary eyewall in Hurricane Rita of 2005. *J. Atmos. Sci.*, *67*, 3581–3599.
764
- 765 Judt, F., & Chen, S. S. (2016). Predictability and dynamics of tropical cyclone rapid
766 intensification deduced from high-resolution stochastic ensembles. *Monthly Weather*
767 *Review*, *144*(11), 4395–4420. <https://doi.org/10.1175/MWR-D-15-0413.1>
768
- 769 Judt, F., Chen, S. S., & Berner, J. (2016). Predictability of tropical cyclone intensity: Scale-
770 dependent forecast error growth in high-resolution stochastic kinetic-energy backscatter
771 ensembles. *Quarterly Journal of the Royal Meteorological Society*, *142*(694), 43–57.
772 <https://doi.org/10.1002/qj.2626>
773
- 774 Katz, R. W., and Murphy, A. H., (2015). *Economic Value of Weather and Climate*
775 *Forecasts*. Cambridge University Press, 240 pp.
776
- 777 Kieu, C. Q., and Moon, Z. (2016). Hurricane intensity predictability. *Bulletin of the American*
778 *Meteorological Society*, *97*(10), 1847–1857. <https://doi.org/10.1175/BAMS-D-15-00168.1>
779

- 780 Kieu, C. and Rotunno, R. (2022). Characteristics of Tropical-Cyclone Turbulence and Intensity
781 Predictability. *Geophysical Research Letters*, 49(8). <https://doi.org/10.1029/2021GL096544>
782
- 783 Kwon, Y. C., Lord, S., Lapenta, B., Tallapragada, V., Liu, Q., and Zhang, Z., (2010). Sensitivity
784 of air-sea exchange coefficients (Cd and Ch) on hurricane intensity. *29th Conf. on Hurricanes*
785 *and Tropical Meteorology*, Tucson, AZ, Amer. Meteor. Soc.,
786 13C.1, https://ams.confex.com/ams/29Hurricanes/techprogram/paper_167760.htm.
787
- 788 Lacis, A. A., and Hansen, J. E., (1974). A parameterization for the absorption of solar radiation
789 in the earth's atmosphere. *J. Atmos. Sci.*, 31, 118–133, [https://doi.org/10.1175/1520-
790 0469\(1974\)031<0118:APFTAO>2.0.CO;2](https://doi.org/10.1175/1520-0469(1974)031<0118:APFTAO>2.0.CO;2).
791
- 792 Li, Q., & Wang, Y. (2012). A comparison of inner and outer spiral rainbands in a numerically
793 simulated tropical cyclone. *Monthly Weather Review*, 140(9), 2782–2805.
794 <https://doi.org/10.1175/MWR-D-11-00237.1>
795
- 796 Lorenz, E. N., (1969). The predictability of a flow which possesses many scales of
797 motion. *Tellus*, 21, 289–307, <https://doi.org/10.3402/tellusa.v21i3.10086>.
798
- 799 Lorenz, E. N., (1996). Predictability—A problem partly solved. *Proc. Seminar on*
800 *Predictability*, Reading, United Kingdom, ECMWF, 1–18.
- 801 Lu, X., Wang, X., Tong, M., & Tallapragada, V. (2017). GSI-based, continuously cycled, dual-
802 resolution hybrid ensemble-variational data assimilation system for HWRF: System description
803 and experiments with edouard (2014). *Monthly Weather Review*, 145(12), 4877–4898.
804 <https://doi.org/10.1175/MWR-D-17-0068.1>
805
- 806 Ma, Z., Fei, J., Liu, L., Huang, X., & Li, Y. (2017). An investigation of the influences of
807 mesoscale ocean eddies on tropical cyclone intensities. *Monthly Weather Review*, 145(4), 1181–
808 1201. <https://doi.org/10.1175/MWR-D-16-0253.1>
809
- 810 Ma, Z., Fei, J., Huang, X., & Cheng, X. (2018). Modulating Effects of Mesoscale Oceanic
811 Eddies on Sea Surface Temperature Response to Tropical Cyclones Over the Western North
812 Pacific. *Journal of Geophysical Research: Atmospheres*, 123(1), 367–379.
813 <https://doi.org/10.1002/2017JD027806>
814
- 815 Moeng, C. H., Dudhia, J., Klemp, J., & Sullivan, P. (2007). Examining two-way grid nesting for
816 large eddy simulation of the PBL using the WRF model. *Monthly Weather Review*, 135(6),
817 2295–2311. <https://doi.org/10.1175/MWR3406.1>
818
- 819 Moller, J. D., & Montgomery, M. T. (2000). Tropical cyclone evolution via potential vorticity
820 anomalies in a three-dimensional balance model. *Journal of the Atmospheric Sciences*, 57(20),
821 3366–3387. [https://doi.org/10.1175/1520-0469\(2000\)057<3366:TCEVPV>2.0.CO;2](https://doi.org/10.1175/1520-0469(2000)057<3366:TCEVPV>2.0.CO;2)
822
- 823 Nystrom, R. G., Zhang, F., Munsell, E. B., Braun, S. A., Sippel, J. A., Weng, Y., & Emanuel, K.
824 (2018). Predictability and dynamics of Hurricane Joaquin (2015) explored through convection-

- 825 permitting ensemble sensitivity experiments. *Journal of the Atmospheric Sciences*, 75(2), 401–
826 424. <https://doi.org/10.1175/JAS-D-17-0137.1>
- 827
- 828 Nolan, D. S., Moon, Y., & Stern, D. P. (2007). Tropical cyclone intensification from asymmetric
829 convection: Energetics and efficiency. *Journal of the Atmospheric Sciences*, 64(10), 3377–3405.
830 <https://doi.org/10.1175/JAS3988.1>
- 831
- 832 Persing, J., Montgomery, M. T., McWilliams, J. C., & Smith, R. K. (2013). Asymmetric and
833 axisymmetric dynamics of tropical cyclones. *Atmospheric Chemistry and Physics*, 13(24),
834 12299–12341. <https://doi.org/10.5194/acp-13-12299-2013>
- 835
- 836 Qin, N., Wu, L., & Liu, Q. (2021). Evolution of the moat associated with the secondary eyewall
837 formation in a simulated tropical cyclone. *Journal of the Atmospheric Sciences*, 78(12), 4021–
838 4035. <https://doi.org/10.1175/JAS-D-20-0375.1>
- 839
- 840 Qin, N., Wu, L., Liu, Q., and Zhou, X., (2023). Driving forces of extreme updrafts associated
841 with convective bursts in the eyewall of a simulated tropical cyclone. *Journal of Geophysical*
842 *Research: Atmospheres (J. Geophys. Res.)*, 128, e2022JD037061.
843 <https://doi.org/10.1029/2022JD037061>
- 844
- 845 Rios-Berrios, R., and R. D. Torn, 2017: Climatological analysis of tropical cyclone intensity
846 changes under moderate vertical wind shear. *Mon. Wea. Rev.*, 145, 1717–
847 1738, <https://doi.org/10.1175/MWR-D-16-0350.1>.
- 848
- 849 Rogers, R. (2010). Convective-scale structure and evolution during a high-resolution simulation
850 of tropical cyclone rapid intensification. *Journal of the Atmospheric Sciences*, 67(1), 44–70.
851 <https://doi.org/10.1175/2009JAS3122.1>
- 852
- 853 Schwarzkopf, M. D., and Fels, S., (1991). The simplified exchange method revisited: An
854 accurate, rapid method for computation of infrared cooling rates and fluxes. *J. Geophys.*
855 *Res.*, 96, 9075–9096, <https://doi.org/10.1029/89JD01598>.
- 856
- 857 Selz, T. (2019). Estimating the intrinsic limit of predictability using a stochastic convection
858 scheme. *Journal of the Atmospheric Sciences*, 76(3), 757–765. [https://doi.org/10.1175/JAS-D-](https://doi.org/10.1175/JAS-D-17-0373.1)
859 [17-0373.1](https://doi.org/10.1175/JAS-D-17-0373.1)
- 860 Shapiro, L. J., & Willoughby, H. E. (1982). The response of balanced hurricanes to local sources
861 of heat and momentum. *Journal of the Atmospheric Sciences*, 39(2), 378–394.
862 [https://doi.org/10.1175/1520-0469\(1982\)039<0378:TROBHT>2.0.CO;2](https://doi.org/10.1175/1520-0469(1982)039<0378:TROBHT>2.0.CO;2)
- 863
- 864 Shin, S., & Smith, R. K. (2008). Tropical-cyclone intensification and predictability in a minimal
865 three-dimensional model. *Quarterly Journal of the Royal Meteorological Society*, 134(636),
866 1661–1671. <https://doi.org/10.1002/qj.327>
- 867
- 868 Sippel, J. A., & Zhang, F. (2008). A probabilistic analysis of the dynamics and predictability of
869 tropical cyclogenesis. *Journal of the Atmospheric Sciences*, 65(11), 3440–3459.
870 <https://doi.org/10.1175/2008JAS2597.1>

- 871
872 Sippel, J. A., & Zhang, F. (2010). Factors affecting the predictability of Hurricane Humberto
873 (2007). *Journal of the Atmospheric Sciences*, 67(6), 1759–1778.
874 <https://doi.org/10.1175/2010JAS3172.1>
875
- 876 Sun, Y. Q., & Zhang, F. (2016). Intrinsic versus practical limits of atmospheric predictability and
877 the significance of the butterfly effect. *Journal of the Atmospheric Sciences*, 73(3), 1419–1438.
878 <https://doi.org/10.1175/JAS-D-15-0142.1>
879
- 880 Tang, B., & Emanuel, K. (2012). Sensitivity of tropical cyclone intensity to ventilation in an
881 axisymmetric model. *Journal of the Atmospheric Sciences*, 69(8), 2394–2413.
882 <https://doi.org/10.1175/JAS-D-11-0232.1>
883
- 884 Tao, D., & Zhang, F. (2015). Effects of vertical wind shear on the predictability of tropical
885 cyclones: Practical versus intrinsic limit. *Journal of Advances in Modeling Earth Systems*, 7(4),
886 1534–1553. <https://doi.org/10.1002/2015MS000474>
887
- 888 Torn, R. D., Whitaker, J. S., Pegion, P., Hamill, T. M., & Hakim, G. J. (2015). Diagnosis of the
889 source of GFS medium-range track errors in Hurricane Sandy (2012). *Monthly Weather*
890 *Review*, 143(1), 132–152. <https://doi.org/10.1175/MWR-D-14-00086.1>
891
- 892 Torn, R. D., Elless, T. J., Papin, P. P., & Davis, C. A. (2018). Tropical cyclone track sensitivity
893 in deformation steering flow. *Monthly Weather Review*, 146(10), 3183–3201.
894 <https://doi.org/10.1175/MWR-D-18-0153.1>
895
- 896 Van Sang, N., Smith, R. K., & Montgomery, M. T. (2008). Tropical-cyclone intensification and
897 predictability in three dimensions. *Quarterly Journal of the Royal Meteorological*
898 *Society*, 134(632), 563–582. <https://doi.org/10.1002/qj.235>
899
- 900 Wang, Y., & Wu, C. C. (2004, December). Current understanding of tropical cyclone structure
901 and intensity changes - A review. *Meteorology and Atmospheric Physics*.
902 <https://doi.org/10.1007/s00703-003-0055-6>
903
- 904 Wu, L., Wang, B., & Geng, S. (2005). Growing typhoon influence on east Asia. *Geophysical*
905 *Research Letters*, 32(18), 1–4. <https://doi.org/10.1029/2005GL022937>
906
- 907 Wu, T. C., Liu, H., Majumdar, S. J., Velden, C. S., & Anderson, J. L. (2014). Influence of
908 assimilating satellite-derived atmospheric motion vector observations on numerical analyses and
909 forecasts of tropical cyclone track and intensity. *Monthly Weather Review*, 142(1), 49–71.
910 <https://doi.org/10.1175/MWR-D-13-00023.1>
911
- 912 Yang, B., Wang, Y., & Wang, B. (2007). The effect of internally generated inner-core
913 asymmetries on tropical cyclone potential intensity. *Journal of the Atmospheric Sciences*, 64(4),
914 1165–1188. <https://doi.org/10.1175/JAS3971.1>
915

- 916 Zhang, B., Lindzen, R. S., Tallapragada, V., Weng, F., Liu, Q., Sippel, J. A., ... Bender, M. A.
917 (2016). Increasing vertical resolution in US models to improve track forecasts of Hurricane
918 Joaquin with HWRF as an example. *Proceedings of the National Academy of Sciences of the*
919 *United States of America*, 113(42), 11765–11769. <https://doi.org/10.1073/pnas.1613800113>
920
- 921 Zhang, D. L., & Chen, H. (2012). Importance of the upper-level warm core in the rapid
922 intensification of a tropical cyclone. *Geophysical Research Letters*, 39(2).
923 <https://doi.org/10.1029/2011GL050578>
924
- 925 Zhang, F., & Tao, D. (2013). Effects of vertical wind shear on the predictability of tropical
926 cyclones. *Journal of the Atmospheric Sciences*, 70(3), 975–983. [https://doi.org/10.1175/JAS-D-](https://doi.org/10.1175/JAS-D-12-0133.1)
927 [12-0133.1](https://doi.org/10.1175/JAS-D-12-0133.1)
928
- 929 Zhang, S., Pu, Z., & Velden, C. (2018). Impact of enhanced atmospheric motion vectors on
930 HWRF Hurricane analyses and forecasts with different data assimilation configurations. *Monthly*
931 *Weather Review*, 146(5), 1549–1569. <https://doi.org/10.1175/MWR-D-17-0136.1>
932
- 933 Zhong, Q., Li, J., Zhang, L., Ding, R., & Li, B. (2018). Predictability of tropical cyclone
934 intensity over the Western North Pacific using the IBTrACS dataset. *Monthly Weather*
935 *Review*, 146(9), 2741–2755. <https://doi.org/10.1175/MWR-D-17-0301.1>
936
- 937 Zhou, X., Zhu, Y., Hou, D., Fu, B., Li, W., Guan, H., ... Pegion, P. (2022). The Development of
938 the NCEP Global Ensemble Forecast System Version 12. *Weather and Forecasting*, 37(6),
939 1069–1084. <https://doi.org/10.1175/waf-d-21-0112.1>
940
941